Modelling of dislocations, twins and crack-tips in HCP and BCC Ti

Tongqi Wen[a], Anwen Liu[b], Rui Wang[b], Linfeng Zhang[c], Jian Han[b], Han Wang[d,*], David J. Srolovitz[a], Zhaoxuan Wu[b,e,**]

[a]*Department of Mechanical Engineering, The University of Hong Kong, Hong Kong SAR, China*
[b]*Department of Materials Science and Engineering, City University of Hong Kong, Hong Kong SAR, China*
[c]*DP Technology, Beijing, China*
[d]*Laboratory of Computational Physics, Institute of Applied Physics and Computational Mathematics, Beijing, China*
[e]*Hong Kong Institute for Advanced Study, City University of Hong Kong, Hong Kong SAR, China*

Abstract

Ti exhibits complex plastic deformation controlled by active dislocation and twinning systems. Understandings on dislocation cores and twin interfaces are currently not complete or quantitative, despite extensive experimental and simulation studies. Here, we determine the dislocation core, twin, and crack properties in both HCP and BCC Ti using a Deep Potential (DP), DFT and linear elastic fracture mechanics. We compute the core structures, critical resolved shear stresses and mobilities of the $\langle\mathbf{a}\rangle$, $\langle\mathbf{c}+\mathbf{a}\rangle$, $\langle\mathbf{c}\rangle$ dislocations in HCP and the $\langle 111\rangle/2$ dislocations in BCC Ti. The $\langle\mathbf{a}\rangle$ slip consists of slow core migration on pyramidal-I planes and fast migration on prism-planes, and is kinetically limited by cross-slips among them. This behaviour is consistent with "locking-unlocking" phenomena in TEM and is likely an intrinsic property. Large-scale DFT calculations provide a peek at the screw $\langle\mathbf{c}+\mathbf{a}\rangle$ core and glide behaviour, which is further quantified using DP-Ti. The screw $\langle\mathbf{c}+\mathbf{a}\rangle$ is unstable on pyramidal-II planes. The mixed $\langle\mathbf{c}+\mathbf{a}\rangle$ is nearly sessile on pyramidal-I planes, consistent with observations of long dislocations in this orientation. The edge and mixed $\langle\mathbf{c}+\mathbf{a}\rangle$ are unstable against a pyramidal-to-basal (PB) transition and become sessile at high temperatures, corroborate the difficulties in $\langle\mathbf{c}\rangle$-axis compression of Ti. Cracks on basal planes are predicted and shown to be intrinsically brittle, consistent with cleavage facets primarily on this plane in experiments. Twin boundary energies vary considerably but all twin boundary structures possess a mirror reflection symmetry. Finally, in BCC Ti, the $\langle 111\rangle/2$ screw has a degenerate core with average glide on $\{112\}$ planes; the $\langle 111\rangle/2$ edge and mixed dislocations have non-dissociated cores on $\{110\}$ planes. This work paints a self-consistent, complete picture on all dislocations in Ti, rationalises previous experimental observations on Ti plasticity and fracture, and points to future HRTEM examinations of unusual dislocations such as the mixed and PB transformed $\langle\mathbf{c}+\mathbf{a}\rangle$ cores.

Keywords: dislocations, crack tip plasticity, twinning, metallic material, molecular dynamics

1. Introduction

Ti has low density, high strength and excellent resistance to corrosion. It exhibits multiple allotropes which can be tuned through alloying and thermo-mechanical processing. These combined properties make it attractive for structure material applications. A wide range of Ti-based alloys have been developed and used extensively in the aerospace (Peters et al., 2003), chemical and biomedical industries (Banerjee and Williams, 2013). For examples, commercially pure HCP-α Ti is widely used as corrosion resistant materials in the petrochemical industry, while the dual-phase Ti-6Al-4V alloy and its derivatives are among the primary materials in constructing load-carrying aircraft structures and engine components. BCC-β Ti is also versatile; its alloys can be heat-treated/precipitate-strengthened to very high strength, or tuned to possess high fatigue strength, low modulus and be bio-compatible (Bahl et al., 2021).

The diversity of Ti applications is well-recognised, so too are the complexities associated with its thermodynamic and mechanical properties. In the HCP structure, Ti exhibits strong elastic (Tesař et al., 2023) and plastic anisotropy (Gong and Wilkinson, 2009). Its plastic deformation is carried out by dislocation slip and accompanied by deformation twinning at low temperatures. Slip via dislocation occurs in the close-packed $\langle\mathbf{a}\rangle$ direction on prismatic, pyramidal I and sometimes basal planes, and in the $\langle\mathbf{c}+\mathbf{a}\rangle$ direction

*Corresponding author
**Corresponding author
Email addresses: wang_han@iapcm.ac.cn (Han Wang), zhaoxuwu@cityu.edu.hk (Zhaoxuan Wu)

on pyramidal I and II planes (Castany et al., 2007; Yu et al., 2013) (Fig. S1a in the Supplementary Materials (SM)). There are four primary deformation twinning modes: (i) $\langle 10\bar{1}1\rangle\{10\bar{1}2\}$, (ii) $\langle 11\bar{2}6\rangle\{11\bar{2}1\}$, (iii)$\langle 11\bar{2}3\rangle\{11\bar{2}2\}$ and (iv) $\langle 10\bar{1}2\rangle\{10\bar{1}1\}$ – the first two modes lead to extension and the latter two to compression in the crystallographic $\langle \mathbf{c}\rangle$ direction (Beyerlein et al., 2014). While each deformation mode is intrinsically different, a wide range of experiments show that their activations and operations are sensitive to alloy compositions (e.g. Al (Williams et al., 2002; Zhang et al., 2019) and oxygen content (Chong et al., 2020; Yu et al., 2015)) and loading conditions (e.g., temperatures and loading direction (Gong and Wilkinson, 2009; Jones and Hutchinson, 1981)), making plastic deformation in HCP Ti highly complex. In addition, HCP Ti exhibits various anomalous behaviours, e.g. shear instability in compression along the $\langle \mathbf{c}\rangle$ axis at high temperatures (Williams et al., 2002), dynamic strain-ageing within some temperature ranges (Marchenko et al., 2016), and cleavage-like crack growth under fatigue loadings (Bache, 2003; Xu et al., 2020; Yazar et al., 2022). Such unusual plastic behaviour may be traced to dislocation core and crack-tip properties; these are not well understood and currently under active investigation.

BCC Ti also exhibits complex elastic and plastic behaviour. Below 1155 K, pure BCC Ti is mechanically unstable as its elastic constants violate the Born criterion ($C_{11} < C_{12}$ (Mouhat and Coudert, 2014)). The BCC structure can be stabilised by entropy (Kadkhodaei et al., 2017) and/or alloying (Bahl et al., 2021) (e.g., V, Mo, Nb, etc). However, the instability of pure BCC Ti at low temperatures makes it difficult to study the intrinsic dislocation and plastic deformation behaviour. In solute-stabilised BCC Ti, plastic deformation is also highly complex; dislocation slip, twinning and martensitic transformation may each be activated, depending on alloy compositions (Bahl et al., 2021) and loading conditions (Gao et al., 2018; Lhadi et al., 2018). In-situ TEM studies suggest that $\langle 111\rangle/2$ screw dislocations can glide on $\{110\}$, $\{112\}$ and $\{123\}$ planes (Fig. S1b in SM) and control plastic deformation in some β-alloys, similar to that in BCC transition metals. However, dislocation behaviour in stable/metastable β-Ti is strongly influenced by the presence of solutes at high concentration (e.g., 23Nb-0.7Ta-2Zr-0.4Si (Castany et al., 2012)). More fundamentally, dislocation core structures remain mysterious in pure β-Ti, and in particular, the screw core is largely unknown, since it is experimentally intractable (Mendis et al., 2006). In addition, some β alloys exhibit unusual plastic behaviour, such as nearly zero work hardening, making them susceptible to plastic instability (e.g., shear localisation during forming).

Given the technological importance and complex plastic behaviour of Ti, extensive theoretical and computational studies have been carried out to investigate its mechanical behaviour. At the macroscopic/meso scales, both viscoplastic phenomenological (e.g., the Khan-Liang-Farrokh (KLF) model (Farrokh and Khan, 2009) and modified Khan–Huang–Liang (KHL) model (Khan and Huang, 1992; Khan and Liang, 1999; Khan and Zhang, 2000)) and mechanism-based (e.g., crystal plasticity, phase field) models have been developed to study the mechanical behaviour of HCP Ti and its alloys in the past. For phenomenological models, the KLF model was shown to accurately capture the stress-strain behaviour of ultrafine-grained/nanocrystalline Ti over a range of grain sizes, strain rates and temperatures (Liu et al., 2015). The modified KHL equation can predict stress-strain behaviour of Ti-6Al-4V alloys under different loading conditions (Khan et al., 2007, 2004). In addition, the KHL model was used to determine the yield parameters of Ti-6Al-4V and a yield criterion was proposed to predict the plastic yield behaviour over a wide range of strain rates and temperatures (Khan et al., 2012). For mechanism-based models, a dislocation-density-based crystal plasticity constitutive model was developed and calibrated for polycrystalline HCP metals. The model reveals the importance of local plastic anisotropy and heterogeneity in flow stress rate-sensitivity of Ti-7Al (Ghosh et al., 2016; Shahba and Ghosh, 2016). With the combination of experiments and a crystal plasticity model for discrete intragranular shear localisation, researchers studied the localised slip bands on the prism planes and $\langle 10\bar{1}2\rangle\{10\bar{1}1\}$ tensile twins and their transmission across grain boundaries (GBs) in commercially pure Ti (CP-Ti) (Ahmadikia et al., 2023). The orientation and curvature of the GB are shown to influence the local stress fields at GBs and slip/twin transmission across the boundary. Recently, polycrystal modelling was used to study the interactions between dislocation slip and twinning in load reversals of CP-Ti (Wang et al., 2020). The polycrystal model includes slip-system level back-stress from accumulations of dislocation density. In addition, a recent phase field model was applied to simulate the motion of individual partial and full dislocations in HCP crystals; this model can predict the partial Burgers vectors, dissociation distances, core widths of the partials in Ti (Albrecht et al., 2020). The above macroscopic/meso scale models significantly enhance our understandings on plastic deformation in HCP Ti. However, they are calibrated with experiments or atomistic calculations for key properties such as the critical resolved shear stresses (CRSS) (Ahmadikia et al., 2023; Iftikhar et al., 2022; Wang et al., 2020) and generalised stacking fault energy curves/surfaces (γ-lines/surfaces) of individual slip systems (Albrecht et al., 2020).

At the microscopic scales, atomistic simulations have been carried out to provide physical insights on

the detailed defect interactions and evolution during plastic deformation (Cheng and Ngan, 2013; Junge and Molinari, 2014; Romero et al., 2022; Wang et al., 2018b). In particular, density-functional theory (DFT) calculations have been performed to determine the core structures of the $\langle \mathbf{a} \rangle$ dislocation on the pyramidal I, prism I and basal planes of HCP Ti (Clouet et al., 2015; Ghazisaeidi and Trinkle, 2012; Kwasniak and Clouet, 2019; Poschmann et al., 2018; Tsuru et al., 2022). The screw $\langle \mathbf{a} \rangle$ dislocation exhibits multiple core structures and the ground state is on the pyramidal I plane. However, the energy differences among different cores are small, on the order of 10 meV/Å, and are sensitive to boundary conditions, valence electrons and k-point meshes in DFT calculations (Poschmann et al., 2018). Combined with *in-situ* TEM study, the screw $\langle \mathbf{a} \rangle$ dislocation was shown to cross-slip between the low-energy pyramidal I and the high-energy prism I plane, exhibiting a rate-limiting "locking-unlocking" process during glide (Clouet et al., 2015). This extreme delicacy of the core structure and energy poses significant challenges for empirical/semi-empirical interatomic potentials in accurately reproducing the screw $\langle \mathbf{a} \rangle$ core structures and glide behaviour (Rida et al., 2022; Wen et al., 2021). Separately, the operation of $\langle \mathbf{c} + \mathbf{a} \rangle$ dislocations is critical in Ti to provide the plastic strain accommodation in the crystallographic $\langle \mathbf{c} \rangle$ direction (in addition to twinning). However, the $\langle \mathbf{c} + \mathbf{a} \rangle$ dislocations have wide core dissociations (Yin et al., 2017), requiring simulation supercells beyond those accessible to routine DFT calculations. Their core structures and glide behaviour have not been determined with first-principle accuracy. In the unstable β-Ti, dislocation core structures cannot be computed at 0 K, so their core properties and glide behaviour remain largely unknown.

While the combined experimental and simulation efforts have shed light on the plastic deformation behaviour in Ti, quantitative understanding is still lacking, particularly on the relevant dislocation core and crack-tip properties. In this work, we leverage a recently-developed machine learning (ML) Deep Potential for Ti (DP-Ti (Wen et al., 2021)), large-scale DFT calculations and linear elastic fracture mechanics theory to study (i) all dislocation core structures and mobilities in both HCP and BCC Ti, (ii) twin interfaces and (iii) crack tip behaviour in HCP Ti, painting a complete, self-consistent picture of dislocation, twin and crack properties in Ti. In particular, we investigate the screw, edge, and/or mixed dislocations ($\langle \mathbf{a} \rangle$, $\langle \mathbf{c} + \mathbf{a} \rangle$, $\langle \mathbf{c} \rangle$ and $\langle 111 \rangle/2$) based on an improved DP-Ti (Wen et al., 2021) and supplemented by DFT. All core dissociations, relative energies and mobilities are quantitatively determined. In addition, we directly demonstrate the "locking-unlocking" phenomenon of the screw $\langle \mathbf{a} \rangle$ dislocation via molecular dynamics (MD) simulations using a large simulation cell and over an extended simulation time. On the pyramidal I plane, screw $\langle \mathbf{c} + \mathbf{a} \rangle$ dislocation core structures are computed and compared in DFT and DP-Ti. Good agreement between these two approaches provides a basis for quantitative measurements of the mobility of $\langle \mathbf{c} + \mathbf{a} \rangle$ dislocations. Furthermore, the $\langle 111 \rangle/2$ screw dislocation is shown to possess a degenerate (D) core in BCC Ti at 1000 K, in agreement with prediction based upon a new material index χ (Wang et al., 2022b). The screw core is also shown to exhibit complex glide behaviour with a mobility lower than its mixed and edge counterparts. Finally, the crack-tip behaviour, dislocation emission vs. cleavage, is determined for a comprehensive set of crack systems in HCP Ti. The current study reveals the intrinsic plastic deformation properties in Ti and provides a basis for understanding plastic behaviour in Ti alloys.

2. Simulation Methods and Models

2.1. Density Functional Theory Calculations

In the current work, DFT calculations are performed using the Vienna *ab initio* simulation package (VASP (Kresse and Furthmüller, 1996)). The generalized gradient approximation (GGA) with Perdew-Burke-Ernzerhof (PBE (Perdew et al., 1996)) parameterization is used for the exchange-correlation functional. The $3d^2 4s^2$ electrons are treated as valence electrons; the rest core electrons are replaced by projector-augmented-wave (PAW (Blöchl, 1994)) pseudopotentials. The cut-off energy of the plane-wave basis is 400 eV. The 1st order Methfessel-Paxton smearing method (Methfessel and Paxton, 1989) is used for partial electron occupancy (smearing width $\sigma = 0.22$ eV). The Monkhorst-pack k-point mesh (Monkhorst and Pack, 1976) is used to sample the Brillouin zone and the linear k-point spacing is kept at 0.2 Å^{-1}.

To compute the dislocation core of the $\langle \mathbf{c}+\mathbf{a} \rangle$ screw dislocation, we first create a fully periodic supercell of HCP lattice with cell vectors $\mathbf{c}_1 = [1\bar{2}13]/3, \mathbf{c}_2 = 10[10\bar{1}0], \mathbf{c}_3 = 20[1\bar{2}10]/3$. The supercell contains 800 atoms (3200 valence electrons). A screw $\langle \mathbf{c}+\mathbf{a} \rangle$ dislocation dipole is introduced at $(0.24\mathbf{c}_2, 0.24\mathbf{c}_3)$ and $(0.76\mathbf{c}_2, 0.76\mathbf{c}_3)$ by displacing atoms according to the anisotropic linear elastic displacement field of the corresponding Volterra dislocations (Anderson et al., 2017). An affine shear deformation is further imposed to compensate the plastic strain induced by the dislocation dipole in the supercell (Bulatov and Cai, 2006). The constructed dislocation cores are optimised using the conjugate gradient algorithm. Convergence is assumed when the energy difference drops below 10^{-4} eV between consecutive steps in both the self-consistency electronic and ionic steps.

2.2. *DP-Ti for Atomistic Modelling*

Plastic deformation in Ti is highly complex as exhibited by various deformation anomalies related to dislocation core and lattice defect properties. Atomistic modelling of dislocations, twins and crack-tips in Ti is necessary but challenging, since empirical and semi-empirical interatomic potentials have limited capabilities in describing the bonding characteristics in different Ti allotropes (ω, α and β). An MEAM interatomic potential (Hennig et al., 2008) and a recent ML Deep Potential (Wen et al., 2021) have been shown to possess the necessary attributes for modelling dislocations in multiphase Ti in a self-consistent manner. In particular, these two potentials accurately capture the cohesive energies, elastic constants and generalised stacking fault energies of both the HCP-α and BCC-β phases. However, previous studies using MEAM show that screw $\langle\mathbf{a}\rangle$ dislocation has lower energy on prism I plane than on pyramidal I plane (Ghazisaeidi and Trinkle, 2012; Poschmann et al., 2018; Rao et al., 2013), which is contradictory to the DFT results. In the current work, we employ an improved version of the Deep Potential for Ti (DP-Ti). DP-Ti is trained using the DeePMD-kit (Wang et al., 2018a) through a workflow consisting of "Initialisation", "DP-GEN loop", and "Specialisation" steps. The detailed training process and benchmarks are described in Wen et al. (2021). Here, we briefly describe the improvements made relative to the earlier version. The current training datasets include additional *ab initio* MD-based 2×2×2 super cells of the ω-phase. In the specialisation-step, the training datasets include segments of the γ-line in the $\langle\mathbf{a}\rangle$ direction on the $\{10\bar{1}0\}$-prism I wide plane and in the $\langle\mathbf{c}+\mathbf{a}\rangle$ direction on the pyramidal II plane (Fig. S1a in SM). The fine-tuned DP-Ti shows properties largely similar to that of the previous DP-Ti. It also exhibits satisfactory agreement with DFT/experiment results on lattice constants and elastic constants at 0 K (Table S1) and finite temperatures (Fig. S7), equation of states (Fig. S3), γ-lines (Figs. S4 and S6) and γ-surfaces (Fig. S5), as well as phase transition temperatures (Fig. S8). The details of generating the ω phase and special datasets, and benchmarks of the current DP-Ti are included in Sec. S3 of SM. The current DP-Ti is compatible with the Large-scale Atomic/Molecular Massively Parallel Simulator (LAMMPS (Thompson et al., 2022)) on both CPU and GPU machines and can thus be readily employed by other interested researchers (DP for Ti at AIS Square, 2023). In addition, the DP compression method (Lu et al., 2022) typically accelerates speeds and reduces memory consumption both by an order of magnitude relative to the original models, enabling large-scale DP-based MD simulations.

2.3. *Molecular Dynamics Simulations*

MD simulations are performed using LAMMPS (Thompson et al., 2022) with DP-Ti via the interface in the DeePMD-kit package (Wang et al., 2018a). We employ cylindrical supercells with a radius R of 100 Å in the dislocation core structure MD simulations. Dislocations are created at the centre of the cylinder with line directions parallel to the cylinder axis. Table S3 in SM summarises the supercell geometries. Specifically, we apply the anisotropic linear elastic displacement to all the atoms according to the corresponding Volterra partial dislocations (Anderson et al., 2017). Atoms within 2 × the cutoff distance ($2r_{\mathrm{c}}$) of DP-Ti from the cylinder outer surface are treated as boundary atoms. The constructed cores are optimised at 0 K with boundary atoms fixed at the elastic displacement solution. Since the $\langle\mathbf{c}+\mathbf{a}\rangle$ edge dislocation line on the pyramidal I plane does not lie along a rational crystallographic direction, we focus on a mixed $\langle\mathbf{c}+\mathbf{a}\rangle$ dislocation aligned in the $\langle\mathbf{a}\rangle$ direction (frequently observed in experiment (Numakura et al., 1986)).

To compare the relative energies of different core dissociations, we calculate the total excessive energy per unit dislocation length in a cylinder of radius r from the core centre as

$$E_{\mathrm{disl}}(r) = E_{\mathrm{total}}(r) - n(r)E_{\mathrm{c}}, \tag{1}$$

where $E_{\mathrm{total}}(r)$ and $n(r)$ are the total potential energy and number of atoms within the cylinder of radius r, and E_{c} is the cohesive energy per atom in the corresponding perfect crystal. The total dislocation energy per unit length may also be expressed as

$$E_{\mathrm{disl}}(r) = E_{\mathrm{core}}(r_{\mathrm{min}}) + K\ln(r/r_{\mathrm{min}}), \tag{2}$$

where $E_{\mathrm{core}}(r_{\mathrm{min}})$ is the near-core energy and $K\ln(r/r_{\mathrm{min}})$ is the elastic energy outside the core region. The near-core energy includes excessive energies associated with the partial core centre, the stacking fault (SF) energy between the partials, their interactions, and thus depends on details of the atomistic structure. $E_{\mathrm{core}}(r_{\mathrm{min}})$ can only be defined with a specific core radius r_{min}; the choice of r_{min} is not unique and depends on the core dissociation width. Here, we choose $r_{\mathrm{min}} \in [4b, 6b, 8b]$, where b is the magnitude of the corresponding Burgers vector (Table S3 in SM). At sufficiently large $r > r_{\mathrm{min}}$, the total dislocation energy scales linearly with $\ln r$. The scaling, energy factor K depends on the material elastic constant tensor $\mathbf{C}$, dislocation Burgers vector $\mathbf{b}$ and line direction $\boldsymbol{\xi}$, i.e., $K(\mathbf{C}, \mathbf{b}, \boldsymbol{\xi})$. Screw dislocations of the

same Burgers vector but different dissociations all have the same K and the total energy difference thus only depends on the near-core energy (core structure and dissociation). The relative energies associated with different dissociations/cores can thus be compared without ambiguity. Edge dislocations can have both different core dissociations and line directions $\boldsymbol{\xi}$. The relative energies have clear physical meanings only when their $\boldsymbol{\xi}$ are the same. In all the cases, K can be computed analytically using anisotropic linear elasticity theory (Anderson et al., 2017) or obtained via fitting to $E_{\text{disl}}(r)$ using Eq. (2). In the current work, we use both methods for cross-validations. Finally, the dislocation core structures are visualised using components of the Nye tensor (Hartley and Mishin, 2005) and the differential displacement (DD) map (Vítek et al., 1970).

2.4. Critical Resolved Shear Stresses and Dislocation Mobilities

Dislocation core structures and energies vary periodically with the lattice periodicity along their glide directions. The energy variation or landscape consists of low energy valleys and high energy ridges. The difference between the valley and ridge is the Peierls barrier ΔE_{PB} which must be overcome during dislocation glide. At 0 K, the applied stress τ_{app} provides the driving force and tilts the energy landscape. With increasing τ_{app}, dislocations may start to glide when ΔE_{PB} is zero and τ_{app} can be taken as the critical resolved shear stress (CRSS) τ_{PS} at 0 K. In the current work, if τ_{PS} is finite, the dislocation is viewed as glissile. If other plastic deformation modes, such as nucleation of other dislocations, cross-slip to other planes, or fracture, occur before dislocation glide, the dislocation can be viewed as sessile in the current configuration. The screw $\langle\mathbf{a}\rangle$ on the pyramidal I plane is special in the sense that it cross-slips to the easy-glide, prism I plane and is considered to be sessile on the pyramidal I plane at 0 K under τ_{app}.

At finite temperatures, the Peierls barrier is overcome by a combination of thermal activation and applied stress. The activation energy under stress can be expressed as

$$\Delta E_{\text{B}} = |\mathbf{b}| \int (\tau_{\text{PS}} - \tau_{\text{app}}) \mathrm{d}A, \tag{3}$$

where $\mathbf{b}$ is the Burgers vector and the integration is carried over the activation area A. When $\tau_{\text{app}} < \tau_{\text{PS}}$, the dislocation velocity is generally written as

$$v = \nu_0 \exp\left(-\frac{\Delta E_{\text{B}}}{kT}\right), \tag{4}$$

where ν_0 is the attempt frequency. Dislocation glide is thus stochastic and depends on τ_{app} or wait time. At finite $\tau_{\text{app}} < \tau_{\text{PS}}$ and infinite wait time, dislocation glide is dominated by thermal activation to nucleate a critical kink and kink propagation. A dislocation will eventually attain a finite velocity at all finite τ_{app}. The CRSS is thus not well-defined; the 0 K definition of τ_{PS} approaches zero at finite temperatures. At $\tau_{\text{app}} > \tau_{\text{PS}}$, dislocation glide can be limited by phonon drag. In this regime, we measure dislocation mobilities based on core positions as a function of time under constant τ_{app}. The dislocation velocity v is the time derivative of the core position. The dislocation mobility m is fitted (Olmsted et al., 2005) as

$$v = |\mathbf{b}|(\tau_{\text{app}} - \tau_0)m, \quad \tau_{\text{app}} \geq \tau_0, \tag{5}$$

where τ_{app} is the shear stress applied in the direction of $\mathbf{b}$ on the slip plane, and τ_0 is viewed as the CRSS of the dislocation above which the glide is athermal. We emphasise that τ_0 is different from the τ_{PS} at zero K. For many dislocations in pure materials, τ_0 is relatively small and rarely controls plasticity. In the current work, we focus on the regime where $\tau_{\text{app}} \geq \tau_0$ and thus τ_0 and the mobility can be established using Eq. 5.

In practice, dislocation mobilities are measured using a supercell consisting of a periodic array of dislocations (PADs (Bulatov and Cai, 2006)). Specifically, we create parallelepiped supercells (Table S3 in SM) and impose periodic boundary conditions in the x and y directions in the glide plane (Fig. S9 in SM). In the z direction, traction-controlled surface boundary conditions are applied. Dislocations are introduced by applying the displacement field of the corresponding Volterra dislocations at the centre of the supercell. For non-pure-edge dislocations, the screw component $\mathbf{b}_{\text{s}}$ is always aligned in x and a homogeneous strain $\varepsilon_{yx} = |\mathbf{b}_{\text{s}}|/2$ is imposed to account for the plastic strain associated with $\mathbf{b}_{\text{s}}$. All constructed supercells are first optimised at 0 K and then equilibrated at target temperatures within an isothermal-isobaric NPT ensemble. The normal stresses are maintained at zero in the x and y directions during the equilibration. To drive the dislocation, a shear stress is created by adding forces in opposite directions along $\mathbf{b}$ on surface layer atoms within 12 Å from the top and bottom surfaces. For the $\langle\mathbf{a}\rangle$ and $\langle\mathbf{c}+\mathbf{a}\rangle$ dislocations in HCP Ti and the $\langle 111\rangle/2$ dislocations in BCC Ti, the applied stresses are first ramped with a step of 5 MPa and 10 MPa and equilibrated for 20 ps between each step increment. The stress-ramping and equilibration process creates various configurations under near-constant stress conditions. For the screw $\langle\mathbf{a}\rangle$ dislocation on the pyramidal I plane, a constant stress of 20 MPa is applied to study the "locking-unlocking" process.

2.5. *Ductile and Brittle Crack Tip Plasticity*

HCP metals such as Mg and Zn exhibit brittle cleavage when deformed at low temperatures or under cyclic loadings. HCP Ti alloys also show quasi-cleavage fracture under fatigue conditions (Xu et al., 2020; Yazar et al., 2022). Brittle fracture is governed by crack tip behaviour, which may be analysed using linear elasticity fracture mechanics (LEFM). Crack tip behaviour is determined by the competition between dislocation emission and brittle cleavage as dictated by their respective critical stress intensity factors (CSIFs). Here, we focus on sharp crack tips under mode-I loading. Specifically, we employ anisotropic linear elasticity, the Rice (Rice, 1992) and Griffith (Griffith, 1921) criteria, and material properties determined using DP-Ti, to compute the CSIFs for dislocation emission and brittle cleavage. The CSIF for cleavage is

$$K_{\mathrm{Ic}} = 2\sqrt{\frac{2\gamma_{\mathrm{surf}} - \gamma_{\mathrm{int}}}{D_{22}(\mathbf{C}, \mathbf{R})}}, \tag{6}$$

where γ_{surf} and γ_{int} are the surface energy of the cleavage plane and the energy of the pre-existing interface (if fracture occurs along an interface), and D_{22} is a parameter that is a function of the elastic tensor $\mathbf{C}$ and crystallographic orientation $\mathbf{R}$ of the crack. D_{22} may be obtained using the Stroh formalism (see Anderson et al. (2017)). The CSIF for dislocation emission is

$$K_{\mathrm{Ie}} = \frac{\sqrt{\gamma_{\mathrm{us}} o(\mathbf{C}, \theta, \mathbf{R})}}{f(\theta, \phi)}, \tag{7}$$

where γ_{us} is the unstable SF energy of the relevant slip system, θ is the angle between the crack and slip plane, and ϕ is the angle between the slip direction and crack front normal. The function o is determined through the Stroh formalism. The functions D_{22}, o and f are described in detail in Sun and Beltz (1994).

In addition, the LEFM predictions are verified in two cases, one for Griffith cleavage and one for dislocation emission using K-field loadings in atomistic simulations with DP-Ti. We use sharp crack configurations in the simulations. Periodic boundary conditions are applied in the crack front z direction. For each case, the crack front (z) length is $\sim$0.5 nm and the other two directions have dimensions of $\sim$80 nm. K-field loading is applied by displacing atoms within $2r_{\mathrm{c}}$ from the remote boundary according to the anisotropic linear elastic displacement field of the sharp crack (see Wu and Curtin (2015a)). We start at an initial K_{I} slightly below K_{Ic} or K_{Ie} and increase the load by ΔK_{I} less than 2% of K_{Ic} or K_{Ie}, followed by structure optimisation with boundary atoms fixed. The plastic response of the sharp crack can thus be modelled explicitly.

3. Dislocations in HCP-α Ti

We first present the core properties of the $\langle \mathbf{a} \rangle$, $\langle \mathbf{c} + \mathbf{a} \rangle$ and $\langle \mathbf{c} \rangle$ dislocations in HCP-α Ti and compare the results with DFT calculations and relevant experimental data. The presented results are from DP-Ti MD simulations if not specified.

3.1. *Dislocation Core Structures and Energies*

Figure 1 shows the core structures and energies of the screw $\langle \mathbf{a} \rangle$ dislocation dissociated on prism I wide and pyramidal I narrow planes. The DD maps are plotted in two variants: $|\mathbf{b}| = a$ and $|\mathbf{b}| = a/2$, to reveal the partial core positions and splitting. For all these cases, the energy pre-factors K_{screw} are identical (within numerical accuracy) and equal to 0.218 eV/Å based on the anisotropic linear elastic theory (Table 1). On the prism I plane (Figs. 1a and b), the two cores have nearly identical energies ($\Delta E_{\mathrm{disl}} < 0.06$ meV/Å) as measured from the atomistic calculations (Eq. (1) and Figs. 1e and f), while the two cores have relatively large energy differences (16.7 meV/Å) on the pyramidal I plane. The screw $\langle \mathbf{a} \rangle$ partials is unstable on the basal $\{0001\}$ plane, spontaneously switching to a pyramidal I plane during structure optimisation at 0 K. The dissociated screw $\langle \mathbf{a} \rangle$ cores and the instability on the basal plane agree well with direct DFT calculations (Clouet et al., 2015; Kwasniak and Clouet, 2019).

We analyse the screw $\langle \mathbf{a} \rangle$ partial cores using fractional Burgers vectors similar to that in BCC structures (Anderson et al., 2017). At each core centre, the partial Burgers vector is resolved through fractional Burgers vectors as

$$\mathbf{b} = \sum_{ij} (\mathbf{u}_{ij} - \mathbf{U}_{ij}) = \sum_{k=1}^{3} \mathbf{d}_k = \mathbf{d}_1 + \mathbf{d}_2 + \mathbf{d}_3, \tag{8}$$

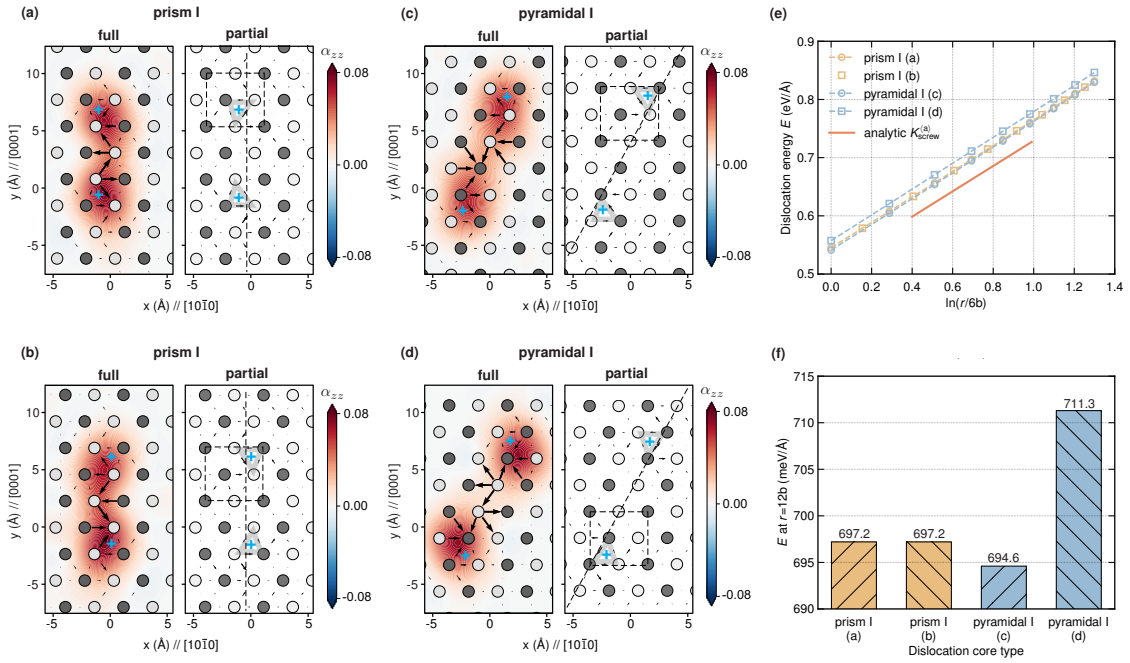

Figure 1: Screw $\langle \mathbf{a} \rangle$ dislocation core structures and energies in HCP Ti. (a-b) Two configurations on the prism I planes. (c-d) Two configurations on the pyramidal I planes. The cores are visualised by the Nye tensor component (α_{zz}, Å^{-1}) and differential displacement vectors. The "+" indicates the partial core position revealed in the DD map calculated by using $|\mathbf{b}| = a/2$. (e) Dislocation energies (a-d) as a function of $\ln(r/6b)$. The slope $K^{\langle a \rangle}_{\text{screw}}$ is calculated using anisotropic linear elasticity theory (Anderson et al., 2017). (f) Dislocation energies (a-d) measured at $r = 12b$. Atom colours (dark and light gray) indicate the AB layers along the viewing $\langle \mathbf{a} \rangle$ direction.

where $\mathbf{u}_{ij}$ and $\mathbf{U}_{ij}$ are the displacement vectors between neighbouring atoms i and j before and after the introduction of the dislocation and $\mathbf{d}_k$ is the DD between atoms i and j. The summation is carried out along an arbitrary path enclosing the dislocation core. Figure 2 shows the atom displacements at the core centres of the respective partial cores in Fig. 1. In the first configuration on the prism I plane (Figs. 1a and 2a-b), the two partial cores (prism I $\mathrm{p_A}$ and prism I $\mathrm{p_B}$) are different; the partial Burgers vectors are resolved as

$$\mathbf{b}^{\text{prism I p}_\text{A}} = \mathbf{d}_1 + \mathbf{d}_2 + \mathbf{d}_3; \tag{9}$$

$$\mathbf{b}^{\text{prism I p}_\text{B}} = \mathbf{d}_4 + \mathbf{d}_6 + \mathbf{d}_5, \tag{10}$$

where the individual measured $\mathbf{d}_i$ projected to $\langle \mathbf{a} \rangle$ are shown in Table 2. In particular, atoms at equivalent core positions have similar DD ($\mathbf{d}_1 \approx \mathbf{d}_4$, $\mathbf{d}_2 \approx \mathbf{d}_6$, $\mathbf{d}_3 \approx \mathbf{d}_5$). The two partial cores thus exhibit subtle differences in their structures, with each corresponding projected $\mathbf{d}_i$ differing slightly in magnitudes. The second configuration on the prism I plane (Fig. 1b) has nearly identical DDs and thus total energy as the first configuration (Figs. 2a-b). We note that it is also possible to obtain configurations with nearly identical partial cores, i.e., $\mathbf{b}^{\text{prism I p}_\text{A}} \approx \mathbf{b}^{\text{prism I p}_\text{B}}$ in the dislocation dipole configuration. Therefore, the partial dissociations exhibit multiple states which are sensitive to the supercell boundary conditions on the prism I plane. Nevertheless, the energy differences are small among all the core dissociations on the prism I plane.

On the pyramidal I plane, the screw $\langle \mathbf{a} \rangle$ dislocation has at least two core dissociations with the lowest and highest energies (Figs. 1c and d), respectively. Both cores dissociate into two partials with some edge components, as indicated in the γ-surface of the pyramidal I plane (Fig. S5 in SM). In both configurations (Figs. 1c and d), the two partial cores are identical and the partial Burgers vectors are resolved as

$$\mathbf{b}^{\text{pyramidal I p}_\text{A}} = \mathbf{d}_7 + \mathbf{d}_8 + \mathbf{d}_9, \tag{11}$$

and

$$\mathbf{b}^{\text{pyramidal I p}_\text{B}} = \mathbf{d}_{11} + \mathbf{d}_{12} + \mathbf{d}_{10}, \tag{12}$$

where the measured fractional Burgers vectors projected in $\langle \mathbf{a} \rangle$ are shown in Table 2.

On the pyramidal I plane, the two partial dissociations are thus distinctly different. Each dissociation has its preferred partial core. Their total energy difference between the two dissociations is thus expected

Table 1: The energy pre-factor K in Eq. (2) computed analytically using anisotropic linear elasticity theory (Anderson et al., 2017) and elastic properties of DP-Ti in comparison with values from linear fitting to $E_{\text{disl}}(r)$ measured in atomistic simulations.

Burgers vector & dislocation type	Slip plane	K_{analytic} (eV/Å)	K_{fitting} (eV/Å)
$\langle \mathbf{a} \rangle$ screw	prism I	0.218	0.221
$\langle \mathbf{a} \rangle$ screw	pyramidal I	0.218	0.222
$\langle \mathbf{a} \rangle$ edge	basal	0.320	0.326
$\langle \mathbf{a} \rangle$ edge	prism I	0.296	0.305
$\langle \mathbf{a} \rangle$ edge	pyramidal I	0.302	0.309
$\langle \mathbf{c}+\mathbf{a} \rangle$ screw	pyramidal I	0.779	0.810
$\langle \mathbf{c}+\mathbf{a} \rangle$ screw	pyramidal II	0.779	0.800
$\langle \mathbf{c}+\mathbf{a} \rangle$ mixed	pyramidal I	1.126	1.105
$\langle \mathbf{c}+\mathbf{a} \rangle$ edge	pyramidal II	1.152	1.155
$\langle \mathbf{c} \rangle$ screw	prism I	0.587	0.599
$\langle \mathbf{c} \rangle$ edge	prism I	0.830	0.794
$\langle \mathbf{c} \rangle$ edge	prism II	0.830	0.793

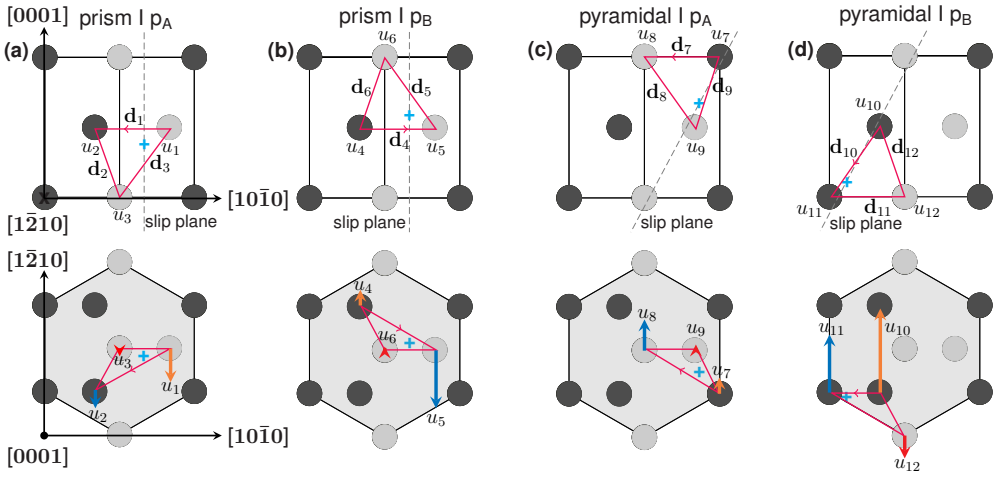

Figure 2: Atom displacements enclosing the various partial screw $\langle \mathbf{a} \rangle$ cores in Fig. 1. In the bottom row figures, the arrows show the atomic displacements in the Burgers vector $\langle \mathbf{a} \rangle$ direction measured in molecular static simulations using DP-Ti. (a-b) Partial dislocation cores on the prism I plane. (c-d) Partial dislocation cores on the pyramidal I plane. Atom colours (dark and light gray) indicate the AB layers along the viewing $\langle \mathbf{a} \rangle$ direction.

Table 2: The magnitudes of the differential displacements (DDs) or fractional Burgers vectors in the $\langle \mathbf{a} \rangle$ direction for the screw $\langle \mathbf{a} \rangle$ dislocation partial cores. See Fig. 2 for the definition of each DD.

	prism I p_A	prism I p_B	pyramidal I p_A	pyramidal I p_B
$\mathbf{d}_i$ projected along $\mathbf{m} = \mathbf{b}/\lvert\mathbf{b}\rvert$	$\mathbf{d}_1 \cdot \mathbf{m}$: -0.158$a$	$\mathbf{d}_4 \cdot \mathbf{m}$: -0.147$a$	$\mathbf{d}_7 \cdot \mathbf{m}$: -0.155$a$	$\mathbf{d}_{11} \cdot \mathbf{m}$: -0.163$a$
	$\mathbf{d}_2 \cdot \mathbf{m}$: -0.122$a$	$\mathbf{d}_6 \cdot \mathbf{m}$: -0.114$a$	$\mathbf{d}_8 \cdot \mathbf{m}$: -0.221$a$	$\mathbf{d}_{12} \cdot \mathbf{m}$: -0.106$a$
	$\mathbf{d}_3 \cdot \mathbf{m}$: -0.220$a$	$\mathbf{d}_5 \cdot \mathbf{m}$: -0.239$a$	$\mathbf{d}_9 \cdot \mathbf{m}$: -0.124$a$	$\mathbf{d}_{10} \cdot \mathbf{m}$: -0.231$a$
Total Burgers vector $\lvert\mathbf{b}\rvert = \lvert\sum \mathbf{d}_i \cdot \mathbf{m}\rvert$	-a/2	-a/2	-a/2	-a/2

to be larger than that of the two cores on the prism I plane with similar partial cores. Since glide of the $\langle \mathbf{a} \rangle$ dislocation passes through these two disparate configurations on the pyramidal I plane, the lattice friction is thus expected to be relatively large as well. This is consistent with direct measurement of the near-core energy (Fig. 1f) and the Peierls stresses of the respective cores (see below).

Comparing the fractional Burgers vectors for the dissociations on the prism and pyramidal planes, we observe that $\mathbf{d}_8$ of $\mathrm{p_A}$ on the pyramidal I plane is very similar to that of the $\mathbf{d}_3$ of $\mathrm{p_A}$ on the prism I plane, while $\mathbf{d}_9$ of $\mathrm{p_A}$ on the pyramidal I plane is very similar to $\mathbf{d}_2$ of $\mathrm{p_A}$ on the prism I plane. The DDs of the low energy partial cores on the pyramidal I plane (Fig. 1c) are thus similar to the $\mathrm{p_A}$ core on the prism I plane (Fig. 1a). However, the DDs of the $\mathrm{p_B}$ core on the pyramidal I plane are quite different from the partial cores on the prism I plane. This further suggests that the screw $\langle \mathbf{a} \rangle$ dislocation dissociation may be controlled by the respective partial core structures and energies, in addition to the metastable SF energies of the prism I and pyramidal I planes.

The energy differences and comparisons with DFT (Clouet et al., 2015; Poschmann et al., 2018; Tsuru et al., 2022) are shown in Table S4 for all cases. The current DP-Ti exhibits the same core energy ordering between the prism and pyramidal dissociations as that in DFT. Quantitatively, DP-Ti under-estimates the energy differences between the low energy pyramidal I dissociation and the low energy prism I dissociation, as well as the energy difference between the two dissociations on the prism I plane. It also over-estimates the energy difference between the high energy dissociation on pyramidal I plane and the high energy dissociation on the prism I plane. Nevertheless, these energy differences are quite small; the corresponding values also vary amongst DFT calculations (Clouet et al., 2015; Poschmann et al., 2018; Tsuru et al., 2022). Convergence criteria, boundary conditions, and simulation supercell sizes may contribute to the 1-2 meV/Å difference amongst DFT calculations, suggesting the extreme delicacy in Ti. Nonetheless, DFT results have the same energy ordering and agree with each other qualitatively overall.

On the pyramidal I plane, the lowest and highest energy core structures in DP-Ti are opposite to that in DFT (Clouet et al., 2015). This discrepancy arises from the deficiency of DP-Ti to accurately capture the energy differences between the individual partial cores (similar to the hard and easy cores in BCC transition metals (Wang et al., 2022a)). This incorrect ordering should not affect pyramidal I plane glide kinetics, since the total energy difference between them are similar to that in DFT (16.7 meV/Å vs. 11-18 meV/Å). On the prism I plane, the two partial dissociations have very close energies and the kinetic barrier to prism I glide is expected to be relatively low (see below). Between the pyramidal I and prism I planes, cross-slip is necessary and the kinetic rate for cross-slips may be studied using DP-Ti. We demonstrate this in the "locking-unlocking" phenomenon which involves the core transition between the two planes. Separately, the dislocation core structures and energies of the edge $\langle \mathbf{a} \rangle$ are included in Sec. S6 in SM.

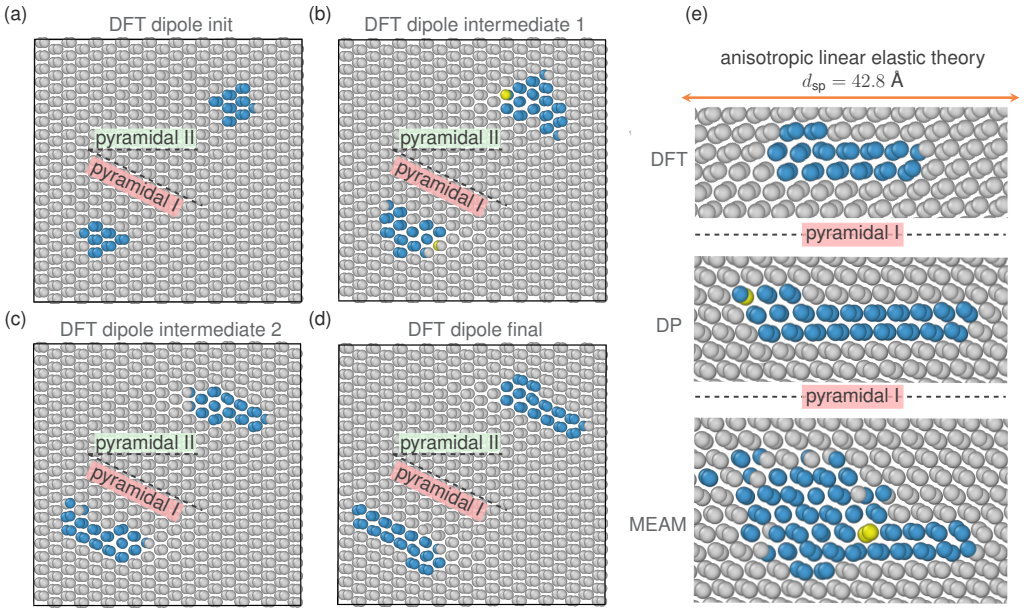

Figure 3: Screw $\langle \mathbf{c}+\mathbf{a} \rangle$ dislocation core structures in HCP Ti. (a-d) Screw $\langle \mathbf{c}+\mathbf{a} \rangle$ dipole dislocation configurations during structure optimisation in DFT. (e) Comparison of the screw $\langle \mathbf{c}+\mathbf{a} \rangle$ dislocation core structure calculated by DFT, DP-Ti, and MEAM (Hennig et al., 2008). Atoms are coloured based on their local atomic environment/structure as identified by the common neighbour analysis (CNA Faken and Jónsson (1994)); HCP: grey, BCC: yellow, others: blue. The partial dislocation separation distance d_{sp} is calculated by anisotropic linear elasticity theory Yin et al. (2017).

Figures 3a-d show the $\langle \mathbf{c}+\mathbf{a} \rangle$ dislocation core evolution in the dipole configuration computed by DFT. During structure optimisation, the initial compact cores spontaneously dissociate onto the pyramidal I planes, forming two pairs of partials with SFs on the pyramidal I planes. The two partials have different core structures, as expected from crystal symmetry. The dissociation process occurs via the glide of the partials in opposite directions along the pyramidal I slip plane as driven by the elastic repulsion between the partial pairs. The dissociation continues with increasing SF widths, driving the two partials of each $\langle \mathbf{c}+\mathbf{a} \rangle$ towards each other at the periodic boundary. While the DFT calculation does not reach to a stable dipole configuration due to this strong dipole interaction and the current supercell size (3200 valence electrons at the limit of DFT), it reveals several critical screw $\langle \mathbf{c}+\mathbf{a} \rangle$ core properties. First, the screw $\langle \mathbf{c}+\mathbf{a} \rangle$ is highly favoured on pyramidal I planes with a well-defined SF, similar to that of HCP Mg (Itakura et al., 2016). Second, both partial cores have relatively compact core centres. Third, both partials are glissile on pyramidal I planes. Figure 3e shows comparisons of the $\langle \mathbf{c}+\mathbf{a} \rangle$ screw cores calculated by DFT, DP-Ti, as well as MEAM (Hennig et al., 2008). The DP-Ti core is very similar to that in DFT; its partial separation appears to be wider but the DFT core is not in an equilibrium configuration. The DP-Ti partial core separation distance is also shorter than the result of anisotropic linear elasticity theory (Yin et al., 2017). This discrepancy is largely due to the higher SF energy of DP-Ti on the pyramidal I plane (see Table S2 in SM). The MEAM core has one partial similar to that of DFT/DP-Ti, while the other partial shows appreciable discrepancies with its core spreading across multiple planes.

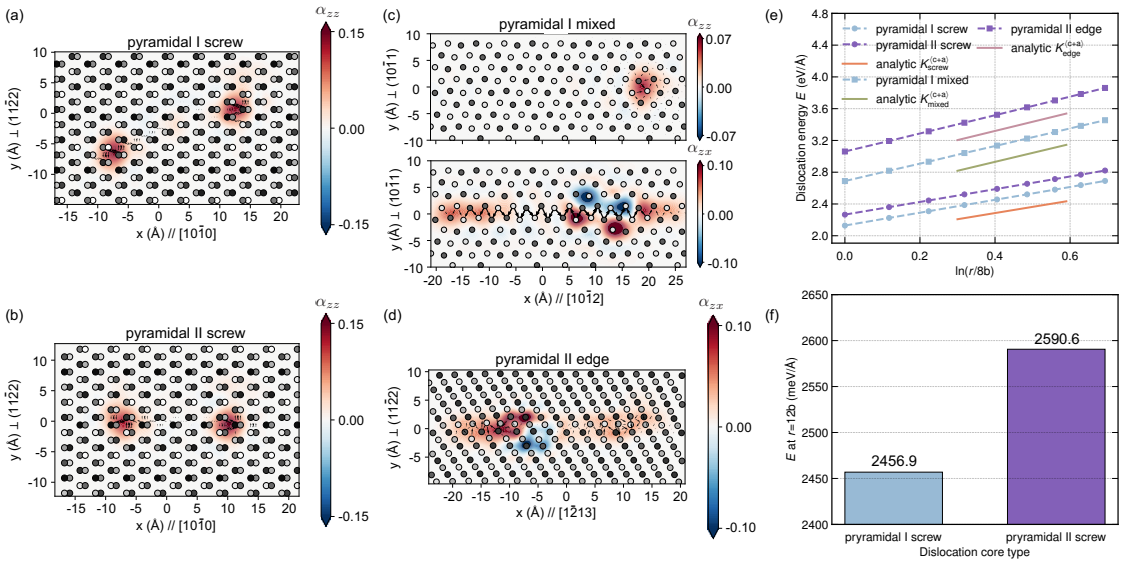

Figure 4: $\langle \mathbf{c}+\mathbf{a} \rangle$ dislocation core structures and energies in HCP Ti. (a-b) Screw $\langle \mathbf{c}+\mathbf{a} \rangle$ dislocation on the pyramidal I and II planes. (c) Mixed $\langle \mathbf{c}+\mathbf{a} \rangle$ dislocation core structure on the pyramidal I plane. α_{zz} and α_{zx} show the screw and edge components, respectively. (d) Edge $\langle \mathbf{c}+\mathbf{a} \rangle$ dislocation on the pyramidal II plane. All cores are visualised by the Nye tensor (α_{zz} and α_{zx}, Å^{-1}) and differential displacement plots. (e) Energy of the $\langle \mathbf{c}+\mathbf{a} \rangle$ dislocations in (a-d) as a function of $\ln(r/8b)$. The slopes $K_{\text{screw/mixed/edge}}$ are calculated using anisotropic linear elasticity theory (Anderson et al., 2017). (f) Energies of the screw $\langle \mathbf{c}+\mathbf{a} \rangle$ dislocations on pyramidal I and II planes at $r = 12b$.

Figure 4 shows the core structures of screw, mixed and edge $\langle \mathbf{c}+\mathbf{a} \rangle$ dislocations predicted by DP-Ti. The screw dislocation dissociates into a pair of partials with a SF on either the pyramidal I or II plane, depending on the initial core construction. When a compact/non-dissociated core is introduced, it always dissociates onto the pyramidal I plane (Fig. 4a), similar to that in DFT (Fig. 3a-d). The pyramidal II dissociation (Fig. 4b) can be obtained by creating a pair of partials of $\langle \mathbf{c}+\mathbf{a} \rangle/2$ separated by $\sim$10 Å on the pyramidal II plane. Both partials have nearly pure screw character and the partial cores are similar, independent of the dissociation plane (Figs. 4a, b). The mixed $\langle \mathbf{c}+\mathbf{a} \rangle$ dislocation dissociates into two partials on the pyramidal I plane (Fig. 4c). The partial core on the right has a mixed character with a screw component of $\langle \mathbf{a} \rangle/2$ aligned on a second pyramidal I plane, resulting in a non-planar partial core, while the left partial core is of pure edge character. The screw component of the right partial is similar to that of a split/saddle core in BCC transition metals (cf. Wang et al. (2022a) and Fig. 4c). This non-planar dissociation may lead to large barriers to the mixed $\langle \mathbf{c}+\mathbf{a} \rangle$ dislocation glide. Finally, the edge dislocation adopts a planar dissociation on the pyramidal II plane; both of its partials are of pure edge character. In all cases, the elastic energy pre-factors K from atomistic simulations agree very well with anisotropic elasticity predictions (Table 1). For the screw $\langle \mathbf{c}+\mathbf{a} \rangle$, the pyramidal II dissociation has a higher total/near-core energy ΔE of 134 meV/Å; this

is nearly an order of magnitude larger than that for the screw $\langle \mathbf{a} \rangle$ dislocation on the pyramidal I and prism I planes. The pyramidal II $\langle \mathbf{c}+\mathbf{a} \rangle$ screw is thus metastable; additional simulations show that it spontaneously cross-slips to the pyramidal I plane at 4 K, consistent with experimental observations where $\langle \mathbf{c}+\mathbf{a} \rangle$ slip is dominant on the pyramidal I plane in pure Ti (Gong and Wilkinson, 2009; Kishida et al., 2020; Numakura et al., 1986; Wang et al., 2013; Zaefferer, 2003). For completeness, the core structures and energies of the $\langle \mathbf{c} \rangle$ dislocations, rarely activated in experiments, are shown in Sec. S7 in SM.

3.2. Critical Resolved Shear Stress and Dislocation Mobility

The above study examines all the possible dislocations in HCP Ti. Overall, the various dislocation cores are largely consistent in DP-Ti and available DFT calculations. For the widely dissociated cores not practical in DFT, DP-Ti also gives results consistent with relevant cases in Mg (Ghazisaeidi et al., 2014) and elasticity. The dissociation planes also agree with the primary slip systems reported in various experiments. We now examine the glide behaviour of the dislocations under driving stresses, both at 0 K and 300 K. We focus on the glissile cores which carry most of the plastic strain.

Table 3: Critical resolved shear stress (τ_0 in MPa) of $\langle \mathbf{a} \rangle$ dislocations measured using DP-Ti and the experimental data.

	Basal plane		**Prism I wide plane**		**Pyramidal I narrow plane**	
Model and temperature	Edge	Screw	Edge	Screw	Edge	Screw
DP-Ti (0 K)	151	∼+1600-1650[1]	277	111	280	>600[5]
DP-Ti (300 K)	<5	<5	<5	<5	<5	∼10-20 MPa[6]
Exp (room temperature)	85;[2] 209[3]		20-50;[4] 181[3]		-	
Exp (200 K)	160[4]		40[4]		-	

[1] The dislocation glides on the pyramidal I plane at high shear stresses on the basal plane.
[2] Simple shear tests of bulk single-crystals of commercially pure HCP-Ti (CP-Ti) (Levine, 1966).
[3] Self-consistent crystal plasticity finite element modelling fitted to data from bending of single crystals CP-Ti micro-cantilever (Gong and Wilkinson, 2009).
[4] Uni-axial tension, uni-axial compression, and simple shear tests of bulk single crystals of CP-Ti (Kishida et al., 2020; Levine, 1966).
[5] The pyramidal core cross-slips to and glides on the prism I plane.
[6] The pyramidal core cross-slips to and glides on the prism I plane at $\tau = 20$ MPa after 520 ps in MD (Fig. 5b).

Table 3 shows the CRSS (τ_{PS} or τ_0) of the $\langle \mathbf{a} \rangle$ dislocations on different slip planes measured using DP-Ti and from experiments of bulk single-crystal HCP-Ti. We note that only CP-Ti samples have been used in experiments and impurities like oxygen can have significant influences on the reported CRSS. In addition, CRSS depends on strain rate at finite temperatures; quantitative comparisons between CRSS from experiments and Eq. (5) are not rigorous and only serve as relative measures among the different slip systems in Ti. The screw $\langle \mathbf{a} \rangle$ is unstable on the basal plane in both DFT (Kwasniak and Clouet, 2019) and DP-Ti. We thus measure the response of the screw $\langle \mathbf{a} \rangle$ dissociated on the pyramidal I plane with a shear stress applied on the basal plane. In experiments, the CRSS (Levine, 1966) can not be unambiguously assigned to individual dislocations of specific characters. At 0 K, the screw dislocation is stationary when the shear stress is applied on the basal plane for stresses below 1600 MPa, above which it glides on the pyramidal I plane. The screw $\langle \mathbf{a} \rangle$ on the prism I wide plane has the lowest CRSS compared to those on basal and pyramidal I planes. This is consistent with the screw partial core structures and relative energetics reported above. Specifically, when the screw $\langle \mathbf{a} \rangle$ glides on the prism I wide plane, its partial cores always pass through similar configurations/local atomic environments with similar energies (Fig. 1a-b). In contrast, when the screw $\langle \mathbf{a} \rangle$ glides on the pyramidal I narrow plane, two metastable partial cores pass through configurations with distinct differences in structures and energies (Fig. 1c-d). This is similar to the saddle and easy cores in BCC structures with large differences in structures and energies. Nonetheless, the saddle core in BCC may be unstable while both cores are at least meta-stable on the pyramidal I narrow plane in HCP Ti. In all cases, the CRSS values have the following order: $\tau^{\text{screw}}_{\text{basal}} > \tau^{\text{screw}}_{\text{pyramidal I}} > \tau^{\text{edge}}_{\text{pyramidal I}} > \tau^{\text{edge}}_{\text{prism I}} > \tau^{\text{edge}}_{\text{basal}} > \tau^{\text{screw}}_{\text{prism I}}$.

The $\langle \mathbf{a} \rangle$ dislocations are highly mobile at 300 K, except for the screw core on the pyramidal I plane. Their CRSSs are negligible compared with those at 0 K. The CRSS values are difficult to extrapolate from fitting to Eq. (5) and should be viewed accurate within a few MPa. In contrast, the screw core appears to be sessile on the pyramidal I plane when the applied shear stress is below 10 MPa. At higher applied stresses and with longer waiting time, it exhibits a "locking-unlocking" behaviour similar to that seen in *in-situ* experiments (Clouet et al., 2015). To further investigate this phenomenon, we perform MD simulations at a lower stress-ramp rate of 25 MPa/ns at 300 K. We use a dislocation of ∼6 nm in length so that the simulation time can be extended to ns time scales. The screw $\langle \mathbf{a} \rangle$ dislocation is constructed on the prism I wide plane, which quickly transforms onto the pyramidal I narrow plane at $\tau_{\text{app}} \approx 0.5$ MPa. Figure 5a

shows the dislocation position and core structure during the stress-ramp process. The dislocation is nearly stationary in the locked configuration for the first 1.2 ns. The pyramidal I core cross-slips to the prism I plane when τ_{app} reaches ∼30 MPa. The cross-slipped core then glides quickly on the prism I plane in the unlocked configuration for stresses from 30 to 35 MPa during the stress ramping.

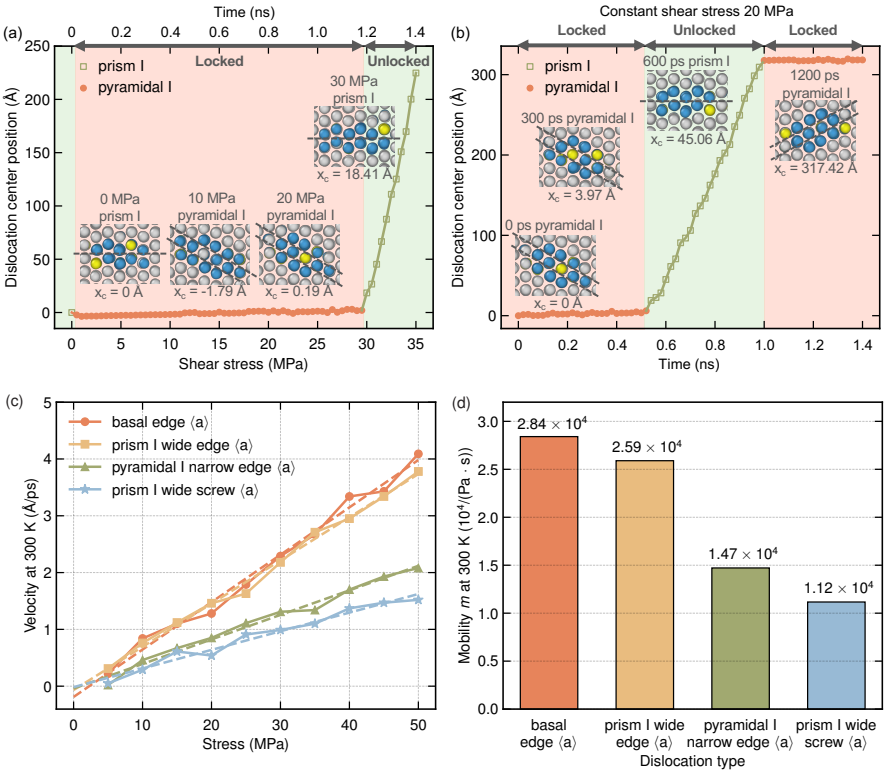

Figure 5: Properties of the $\langle \mathbf{a} \rangle$ dislocations in HCP Ti determined in MD simulations at 300 K. (a) Unlocking of the screw $\langle \mathbf{a} \rangle$ from the pyramidal I plane to the prism plane during stress ramping. (b) "Locking-unlocking" of the screw $\langle \mathbf{a} \rangle$ at a constant applied shear stress of 20 MPa. The insets show different core structures under different stresses or at different simulation times. Atoms are coloured based on their local atomic environment/structure as identified by the common neighbour analysis, CNA (Faken and Jónsson, 1994); HCP: grey, BCC: yellow, others: blue. (c) Dislocation velocities as a function of applied shear stress. (d) Dislocation mobilities m fitted according to Eq. (5).

To investigate the core transition in detail, we perform MD simulations at a constant τ_{app} of 20 MPa at 300 K. The dislocation core is initially dissociated on the pyramidal I plane, similar to that in Fig. 5a. The entire dislocation is nearly stationary with one of its partial core wandering to the next available core position (Fig. 1). The effective velocity is 1.3×10^{-5} Å/ps. The pyramidal I core thus corresponds to the "locked" configuration of the screw $\langle \mathbf{a} \rangle$. At $t \approx 520$ ps (520000 time steps), the pyramidal I core cross-slips to the prism I plane (Fig. 5b) and glides at a nearly constant speed of 0.6 Å/ps, which corresponds to the unlocked core configuration. At $t \approx 988$ ps, the gliding dislocation cross-slips back to the pyramidal I plane and becomes stationary again, i.e., transforms to the "locked" core.

In the *in-situ* TEM straining experiments (Clouet et al., 2015), the screw $\langle \mathbf{a} \rangle$ dislocation appeared locked on the pyramidal I plane for several seconds, followed by a quick glide on the prism I plane. At least two factors may contribute to the discrepancy in time scales between experiments and the MD simulations. First, the temperatures are different in the experiment and MD simulations: the experiment at 150 K, and MD simulation at 300 K. MD simulations are also performed at 150 K but no "locking-unlocking" transition is observed within 2 ns; the waiting time required for core transition at 150 K is beyond the time scale accessible by current MD simulations. The higher temperature in MD simulations should in principle make the core transform occur at higher rates. Second, the sample sizes are different in the simulations and experiment. Although we have used a large supercell with over 0.15 million atoms and a dislocation line of ∼6 nm, this supercell is still much smaller than the experimental sample. Dislocation core transitions occur stochastically and longer dislocation length may favour the transition to shorter waiting times since each segment can act as independent nucleation sites for the transition. The waiting and gliding times may not be quantitatively comparable between the simulations and experiments. Nevertheless, this "locking-

unlocking" mechanism in MD should be similar to that in the *in-situ* TEM (Clouet et al., 2015) and is likely an intrinsic behaviour of the screw $\langle \mathbf{a} \rangle$ dislocation in Ti (without oxygen or other interstitial effects).

Figures 5c-d show the velocities and mobilities of the $\langle \mathbf{a} \rangle$ dislocations measured in MD simulations at 300 K. On the pyramidal I plane, the screw $\langle \mathbf{a} \rangle$ dislocation mobility cannot be unequivocally determined as it cross-slips to the prism I plane at high stresses (Fig. 5a). The screw dislocation is not stable on the basal plane, as discussed earlier. For the remaining cases, the velocity increases nearly linearly with increasing applied stresses, allowing the mobility to be fitted robustly using Eq. (5). The edge $\langle \mathbf{a} \rangle$ dislocation on the basal plane has the highest mobility, followed closely by the edge $\langle \mathbf{a} \rangle$ dislocation on the prism I wide plane. The mobility of the edge dislocation on the pyramidal I narrow plane is nearly half of the previous two cases, while the screw $\langle \mathbf{a} \rangle$ on the prism I wide plane has the lowest mobility. Among all the cases, the dislocation mobilities are of the same order of magnitude and the differences are less drastic compared to those in BCC transition metals (Yin et al., 2021).

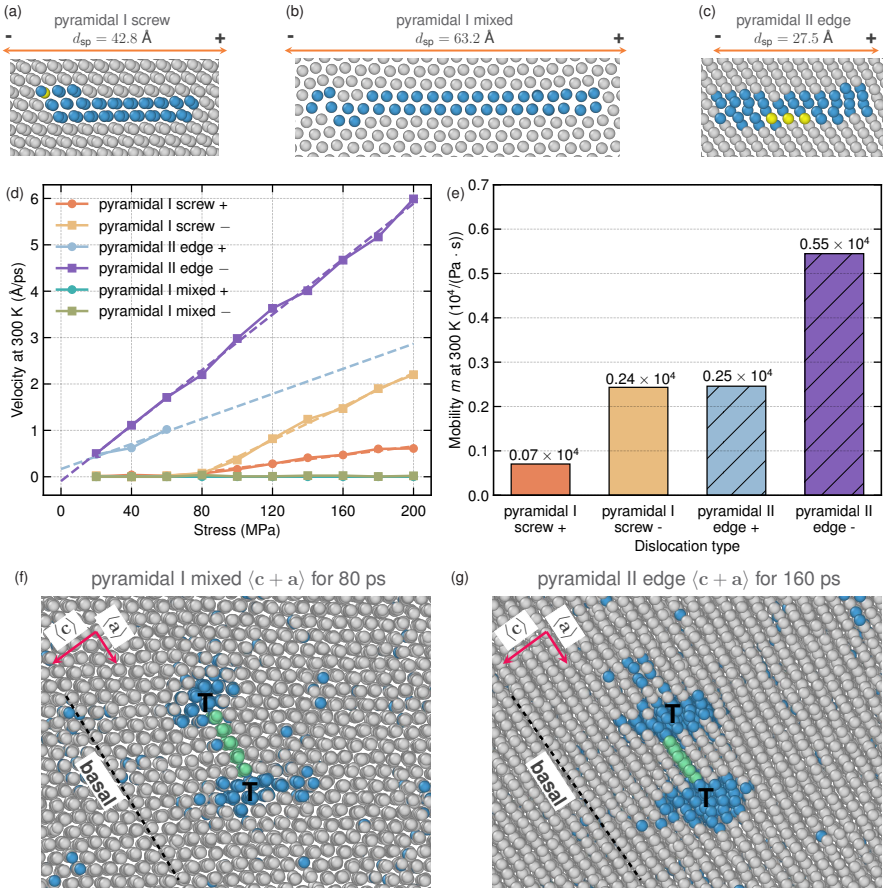

Figure 6: Properties of $\langle \mathbf{c} + \mathbf{a} \rangle$ dislocations at 300 K and 900 K in MD simulations. (a-c) Conventions of the positive and negative shear. d_{sp} is the partial dislocation separation calculated by anisotropic linear elasticity theory (Yin et al., 2017). (d) Dislocation velocity as a function of applied shear stress. (e) Mobility m from fitting the simulation data according to Eq. (5). (f) Climb-dissociation of the mixed $\langle \mathbf{c} + \mathbf{a} \rangle$ dislocation from the pyramidal I to the basal plane after 80 ps. (g) Climb-dissociation of the edge $\langle \mathbf{c} + \mathbf{a} \rangle$ dislocation from the pyramidal II to the basal plane after 160 ps. See Fig. 5 for the atom colour scheme.

Table 4 shows the CRSS of $\langle \mathbf{c} + \mathbf{a} \rangle$ dislocations calculated by DP-Ti. The two partials have different Burgers vectors, so are their core structures and responses to applied stresses. In particular, dislocations exhibit directionality in their glides, as suggested from the asymmetrical γ-lines in the $\langle \mathbf{c} + \mathbf{a} \rangle$ direction on the pyramidal planes (Fig. S4d-e). Figures 6a-c show the positive/negative direction convention used here. At 0 K, the mixed $\langle \mathbf{c}+\mathbf{a} \rangle$ exhibits very high CRSSs in both directions. The screw $\langle \mathbf{c}+\mathbf{a} \rangle$ can glide smoothly in both directions on the pyramidal I plane; the CRSSs differ by 221 MPa between the two directions. In contrast, the $\langle \mathbf{c} + \mathbf{a} \rangle$ screw dislocation is unstable on the pyramidal II plane under τ_{app}, while the $\langle \mathbf{c} + \mathbf{a} \rangle$ edge can glide in both directions with a CRSS difference of 16 MPa. At 300 K, the mixed $\langle \mathbf{c} + \mathbf{a} \rangle$ hardly moves at $\tau_{\text{app}} = 200$ MPa in the positive and negative directions. The CRSSs of the screw decrease by nearly an order of magnitude and the directionality is substantially reduced.

Figures 6d-e show the mobilities of the $\langle \mathbf{c} + \mathbf{a} \rangle$ dislocations. The edge dislocation is highly mobile on

Table 4: Critical resolved shear stress (τ_0 in MPa) of $\langle \mathbf{c}+\mathbf{a} \rangle$ dislocation measured from experiments and calculated by DP-Ti.

	Pyramidal I plane		**Pyramidal II plane**	
Model and temperature	Mixed	Screw	Edge	Screw
DP-Ti (0 K)	∼+1200-1400 -1117	+621 -842	+523 -507	not stable
DP-Ti (300 K)	>+200 ∼-200	+60 -76	not stable[4]	not stable
Exp (room temperature)	474[1]; 580-635[2] 765[3]		-	

[1] Self-consistent crystal plasticity finite element modelling fitted to data from bending of single crystals CP-Ti micro-cantilever (Gong and Wilkinson, 2009).
[2] Uni-axial compression of [0001]-oriented single crystal CP-Ti micro-pillar (Kishida et al., 2020).
[3] Uni-axial compression of [0001]-oriented single crystal Ti-5Al micro-pillar (Yu et al., 2013).
[4] When edge $\langle \mathbf{c}+\mathbf{a} \rangle$ moves in the positive direction at 300 K, it will dissociate on basal plane at the shear stress higher than 65 MPa, similar to that in Figs. 6f and g.

the pyramidal II plane; its mobility is the highest in the negative direction and is reduced by 50% in the positive direction. Furthermore, the edge $\langle \mathbf{c}+\mathbf{a} \rangle$ is not stable at 300 K and dissociates onto the basal plane when τ_{app} is above 65 MPa. The screw $\langle \mathbf{c}+\mathbf{a} \rangle$ exhibits a distinct threshold stress (taken as the CRSS τ_0) below which the dislocation is nearly stationary. Above τ_0, the velocity is proportional to the net shear stress $\tau_{\text{app}} - \tau_0$. Its mobility also has strong directionality; the value in the negative direction is nearly 3.5 times of that in the positive direction (Fig. 6e). The mixed dislocation has a very low velocity ($< 4 \times 10^{-6}$ Å/ps) and the mobility is almost 0 for $\tau_{\text{app}} < 200$ MPa. In all the cases, the edge $\langle \mathbf{c}+\mathbf{a} \rangle$ has the highest mobility on the pyramidal II plane, followed by the screw $\langle \mathbf{c}+\mathbf{a} \rangle$ and mixed $\langle \mathbf{c}+\mathbf{a} \rangle$ on the pyramidal I plane.

The above results show that the edge (under positive shear) and screw (under both positive and negative shears) $\langle \mathbf{c}+\mathbf{a} \rangle$ dislocations are unstable on the pyramidal II plane at room temperature. It is thus difficult to sustain $\langle \mathbf{c}+\mathbf{a} \rangle$ slip on the pyramidal II plane in HCP Ti, leaving the pyramidal I plane as the primary slip plane for $\langle \mathbf{c}+\mathbf{a} \rangle$ dislocations, which is consistent with a wide range of experimental observations (Gong and Wilkinson, 2009; Kishida et al., 2020; Numakura et al., 1986; Wang et al., 2013; Zaefferer, 2003). Furthermore, on the pyramidal I plane, the mixed $\langle \mathbf{c}+\mathbf{a} \rangle$ shows a much lower mobility relative to the pure screw $\langle \mathbf{c}+\mathbf{a} \rangle$. Consequently, the mixed $\langle \mathbf{c}+\mathbf{a} \rangle$ should be the primary dislocations observed in experiments - also consistent with a previous TEM study (Numakura et al., 1986) and a recent *in-situ* TEM observation where $\langle \mathbf{c}+\mathbf{a} \rangle$ dislocations bow out from a tangle of $\langle \mathbf{a} \rangle$ dislocations and some straight $\langle \mathbf{c}+\mathbf{a} \rangle$ segments are stationary or pinned (Yu et al., 2013).

Finally, we examine the high temperature stability of the $\langle \mathbf{c}+\mathbf{a} \rangle$ mixed and edge dislocations on the pyramidal I and II planes. An earlier dislocation energetic analysis (Wu et al., 2016) suggests that $\langle \mathbf{c}+\mathbf{a} \rangle$ dislocations are not stable against climb dissociations on the basal plane in all HCP structures. Figures 6f-g show the two dislocations obtained in MD simulations at 900 K. In both cases, the dislocations are first constructed on their respective pyramidal planes and are stable for ∼30 and ∼40 ps. The two dislocations then spontaneously undergo a climb-dissociation to the final basal-dissociated configurations with no stresses applied. This climb-dissociation is similar to that seen in HCP Mg (Wu and Curtin, 2015b, 2016a). The climb-dissociated cores have lower energies than their pyramidal-dissociated counterparts. In the climb-dissociated configurations, the two partials reside on different pyramidal planes and are connected by an I_1 SF on the basal plane. The transformed $\langle \mathbf{c}+\mathbf{a} \rangle$ dislocation is sessile, which reduces the mobile $\langle \mathbf{c}+\mathbf{a} \rangle$ dislocation density and provides barriers to other $\langle \mathbf{c}+\mathbf{a} \rangle$ on the pyramidal planes. This intrinsic transformation and the presence of sessile cores inhibit further $\langle \mathbf{c}+\mathbf{a} \rangle$ slip and may explain the anomalous shear instability of HCP Ti when compressed along the $\langle \mathbf{c} \rangle$ axis at high temperatures (Williams et al., 2002).

3.3. Twin Boundary Structures and Energies

Deformation twinning is one of the primary deformation mechanisms in HCP Ti. It becomes prevalent with decreasing temperature (Zhao et al., 2021). Figure 7 shows 5 optimised, coherent twin boundary (TB) structures predicted by DP-Ti. Table 5 shows their energies in comparison with DFT results (Hooshmand et al., 2017; Kumar et al., 2015) and a previous MEAM potential. The first 4 TBs are observed in experiments, while the last one on the $\{10\bar{1}3\}$ plane was reported recently (Hooshmand et al., 2017; Kumar et al., 2015). We focus on the results from Hooshmand et al. (2021) since similar valence states (10 valence electrons vs. 12) are used in their DFT calculations and the training datasets of the current DP-Ti. Among the different cases in both DP-Ti and DFT, the TB energies vary substantially; the $\{10\bar{1}1\}$ TB boundary has the lowest energy, nearly at $1/3$ that of the $\{11\bar{2}2\}$ TB. All TBs have a mirror reflection symmetry, in contrast to that in group VB BCC transition metals and Fe where a near-isosceles TB structure is the ground state (Xiao

et al., 2023). In addition, DP-Ti reproduces all TB energies within ∼10% from the respective DFT values and are appropriate for future MD studies of deformation twin nucleation, growth and interactions with dislocations in HCP Ti.

Table 5: Twin boundary energies calculated by DFT and DP-Ti.

	Twin boundary energy γ_{int} (mJ/m^2)				
	$\{10\bar{1}2\}$	$\{11\bar{2}1\}$	$\{11\bar{2}2\}$	$\{10\bar{1}1\}$	$\{10\bar{1}3\}$
DFT	297.6[1], 308.4[2], 330[3]	233.2[4], 273.1[3]	377.1(this work), 385[3]	75.3[1], 100.3[2], 119.4[3]	326.5[1], 345.1[2]
DP-Ti	276.4	226.8	350.1	126.5	318.4
MEAM	178.3	127.0	316.4	112.9	327.9

[1] Kumar et al. (2015)
[2] Hooshmand et al. (2017)
[3] Hooshmand et al. (2021)
[4] Lane et al. (2011)

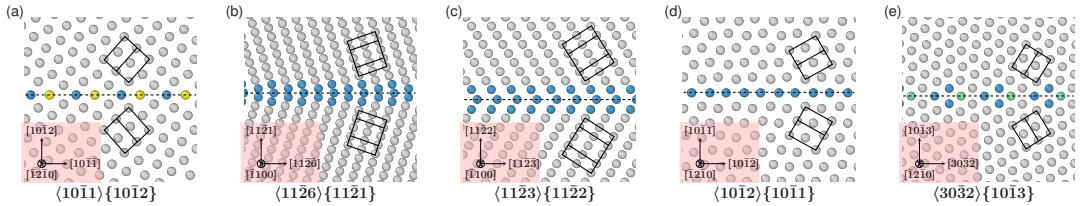

Figure 7: The optimised twin boundary structures in HCP-Ti using DP-Ti. See Fig. 5 for the atom colour scheme.

3.4. Crack-tip Behaviour

Table 6: Crack tip cleavage/emission competition in HCP Ti as predicted from anisotropic linear elastic fracture mechanics. $(\mathbf{n})$ is the crack plane and $[\mathbf{l}]$ is the crack front direction.

Crack plane	**Orientation** $(\mathbf{n})[\mathbf{l}]$	**Slip system**	γ_{surf} (mJ m^{-2})	γ_{us} (mJ m^{-2})	K_{Ic} (MPa m$^{1/2}$)	K_{Ie} (MPa m$^{1/2}$)	**Tip behaviour prediction**
prism wide	$(\bar{1}010)[1\bar{2}10]$	basal $\langle\mathbf{a}\rangle$	1932	390	0.769	0.682	basal $\langle\mathbf{a}\rangle$
	$(\bar{1}010)[0001]$	prism $\langle\mathbf{a}\rangle$	1932	336	0.750	0.589	prism $\langle\mathbf{a}\rangle$
	$(\bar{1}2\bar{1}0)[\bar{1}010]$	basal $\langle\mathbf{a}\rangle$	1986	390	0.780	0.756	basal $\langle\mathbf{a}\rangle$
	$(\bar{1}2\bar{1}0)[0001]$	prism $\langle\mathbf{a}\rangle$	1986	336	0.760	0.625	prism $\langle\mathbf{a}\rangle$
pyramidal I wide	$(10\bar{1}1)[1\bar{2}10]$	basal $\langle\mathbf{a}\rangle$	1823	390	0.749	0.666	basal $\langle\mathbf{a}\rangle$
pyramidal II	$(11\bar{2}2)[\bar{1}100]$	basal $\langle\mathbf{a}\rangle$	2008	390	0.787	0.750	basal $\langle\mathbf{a}\rangle$
	$(11\bar{2}2)[11\bar{2}\bar{3}]$	prism $\langle\mathbf{a}\rangle$	2008	336	0.777	0.701	prism $\langle\mathbf{a}\rangle$
basal	$(0001)[1\bar{2}10]$	pyramidal I $\langle\mathbf{c}+\mathbf{a}\rangle$	1911	611	0.775	**0.837**	**cleavage**
	$(0001)[\bar{1}010]$	pyramidal II $\langle\mathbf{c}+\mathbf{a}\rangle$	1911	623	0.775	**0.839**	**cleavage**
Twin interface	$(10\bar{1}2)[\bar{1}2\bar{1}0]$	basal $\langle\mathbf{a}\rangle$	1894	390	0.738	**0.789**	**cleavage**
	$(10\bar{1}2)[1\bar{2}10]$	basal $\langle\mathbf{a}\rangle$	1894	390	0.752	**2.125**	**cleavage**

Table 6 shows the computed CSIFs for dislocation emission and cleavage using Eqs. (6) and (7). We consider 11 crack systems; 9 on different crystallographic planes and 2 on the $\{10\bar{1}2\}$ tensile twin interface commonly observed in experiments. The potential dislocation slip systems are selected based on γ_{us} and their favourable crystallographic orientations with respect to the crack-tip stress field, i.e., those with the largest resolved shear stresses. In particular, the barriers γ_{us} to nucleating the left and right $\langle\mathbf{c}+\mathbf{a}\rangle$ partials are largely different on the pyramidal planes (Fig. S4d-e); the most favourable, lower γ_{us} is considered here. All cracks on the prism, pyramidal I and II planes are predicted to be intrinsically ductile; i.e., $K_{\text{Ie}} < K_{\text{Ic}}$. For the two cracks on the basal plane, $K_{\text{Ie}} > K_{\text{Ic}}$ and brittle cleavage is predicted to occur prior to emission of $\langle\mathbf{c}+\mathbf{a}\rangle$ dislocations. Cracks on the basal plane appear to be *intrinsically* brittle in HCP Ti; while this is unexpected, it is consistent with experimental observations where quasi-cleavage is commonly seen on the basal plane (Bache, 2003; Xu et al., 2020). The two cracks on the twin interface are also brittle. The $(10\bar{1}2)[\bar{1}2\bar{1}0]$ crack has K_{Ie} marginally larger than K_{Ic}; hence the prediction is not definitive. The $(10\bar{1}2)[1\bar{2}10]$ is intrinsically brittle, largely due to the unfavourable slip system orientation and common in

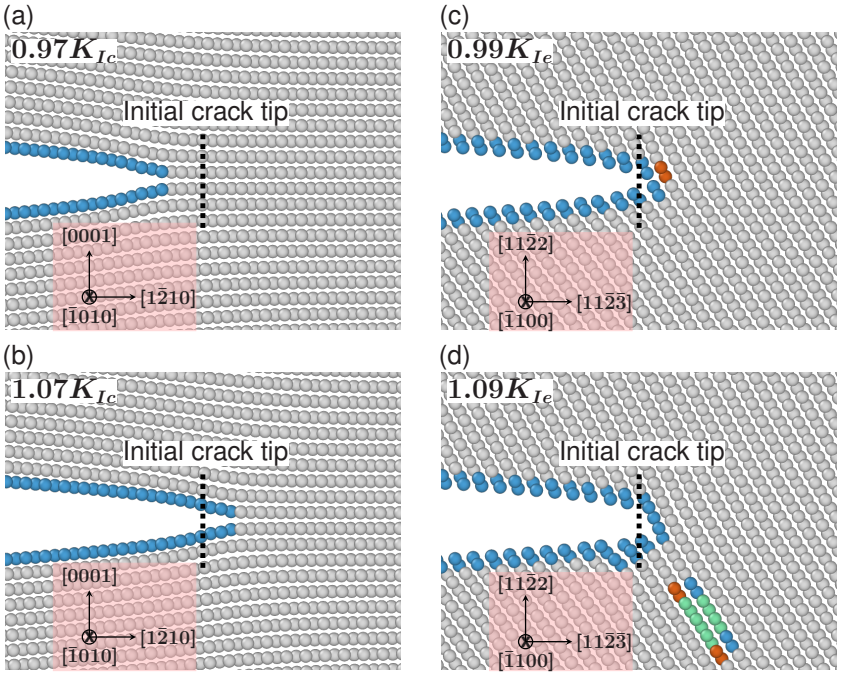

Figure 8: Cross-sectional view of sharp cracks at different K_{I}. The initial crack tip position is determined from the anisotropic elastic solution at a K_{I} slightly below K_{Ic} or K_{Ie}. (a,b) Crack plane (0001) and crack front direction $[\bar{1}010]$ show the Griffith cleavage. (c,d) Crack plane $(11\bar{2}2)$ and crack front direction $[\bar{1}100]$ show the edge $\langle\mathbf{a}\rangle$ dislocation emission. See Fig. 5 for the atom colour scheme.

other crystal structures including the FCC as well. Overall, most cracks in HCP Ti are intrinsically ductile, in stark contrast to that in HCP Mg (Wu and Curtin, 2015a).

Figure 8 shows the crack tip behaviour under mode-I loadings. The $(0001)[\bar{1}010]$ crack (Figs. 8a-b) closes and advances for K_{I} slightly below and above its K_{Ic}, respectively. This basal plane crack thus exhibits Griffith cleavage. In contrast, an edge $\langle\mathbf{a}\rangle$ dislocation is emitted on the basal plane at the tip of the $(11\bar{2}2)[\bar{1}100]$ crack, which in turn blunts the sharp crack tip and exhibits an intrinsically ductile behavior. The direct atomistic simulations are in qualitative agreement (ductile vs. brittle) with the LEFM predictions. Quantitatively, the respective CSIFs are also within 10% from the predictions; these differences are similar to those in FCC metals (Andric and Curtin, 2017). The results are thus robust and reveal the intrinsic behaviour in HCP-Ti.

4. Dislocations in BCC-β Ti

4.1. Dislocation Core Structures

HCP-α Ti is stable at moderate temperatures and transforms to BCC-β Ti at 1155 K under zero pressure conditions (Banerjee and Williams, 2013). The BCC structure is unstable at 0 K. It is thus challenging to study dislocation core properties in BCC-Ti in DFT or experiments. The current DP-Ti predicts a HCP to BCC phase transition at 1252 K under zero stress, similar to that in experiment (Fig. S8 in SM). In addition, DP-Ti also accurately reproduces the generalised SF energy lines, including the negative SF energies on the $\{110\}$, $\{112\}$ and $\{123\}$ planes (Fig. S6 in SM). Hence, this potential is appropriate for studying the dislocation properties in BCC-Ti. Figure 9 shows the core structures of $\langle 111\rangle/2$ dislocations at 1000 K, where the BCC structure is metastable ($C_{11} = 110$ GPa, $C_{12} = 94$ GPa, $C_{44} = 37$ GPa) and relatively clear core structures can be determined. The core structures are obtained using atom positions averaged over 5 ps (5000 time steps). The differential displacement (DD) map (Fig. 9a) shows that the screw core adopts the degenerate (D) structure, in stark contrast to the non-degenerate (ND) core in pure BCC transition metals such as V, Nb, Ta, Cr, Mo and W, but similar to that in BCC Li computed in DFT (Wang et al., 2022b) and a new interatomic potential (Qin et al., 2022). The D core is also consistent with the prediction based on a recent material index χ applicable to all BCC structures. In particular, the ND core is favoured when the energy difference ΔE between the close-packed structure (FCC/HCP) and BCC structure is large while the D core is favoured when ΔE is small. At finite temperatures, the energy difference ΔE should be replaced by the free energy difference ΔF. At 1000 K, close to the phase transition temperature, the free energy

difference ΔF is $\sim$10 meV/atom, much smaller than those in the BCC transition metals (138 meV/atom $<$ ΔE $<$ 483 meV/atom) at 0 K where the ND core is highly favoured.

We further investigate the gliding behaviour of the screw dislocation under a constant shear stress of 160 MPa at 1400 K. Figure 9e shows the screw dislocation core positions taken at 2 ps interval within 40 ps in MD simulations. The screw core glides on different $\{110\}$ planes along a $\{112\}$ mean glide plane. This glide behaviour is consistent with the behaviour of the D core in BCC Lithium at 4 K (Qin et al., 2022). The D core structure is thus fully consistent with the prediction and observed glide behaviour.

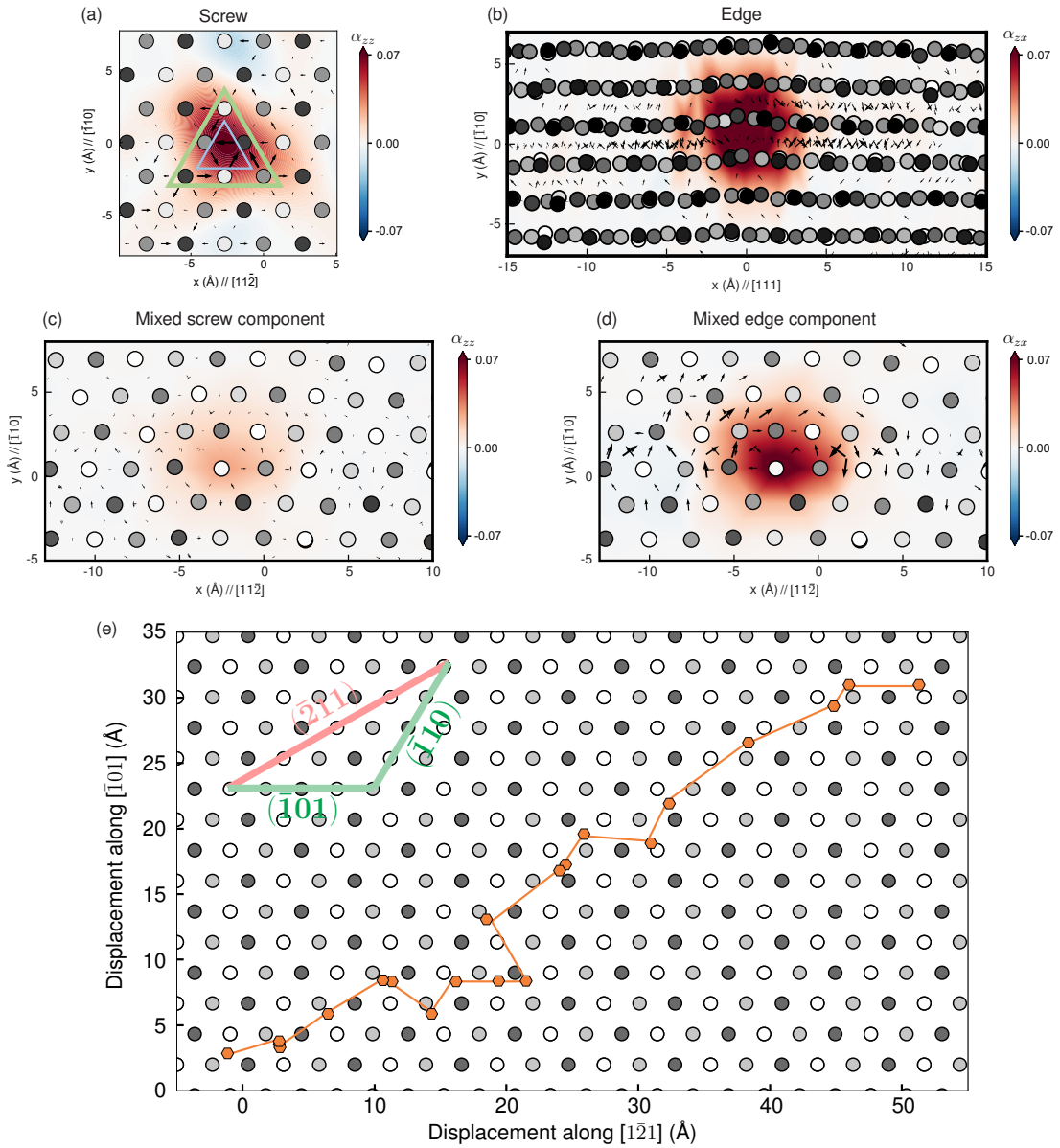

Figure 9: Core structures of the $\langle 111 \rangle/2$ dislocations at 1000 K and $\langle 111 \rangle/2$ screw dislocation glide behaviour at 1400 K obtained in MD simulations using DP-Ti. (a) Degenerate core structure of the screw dislocation. (b) Edge dislocation core. (c-d) Screw and edge component of 70.5° mixed dislocation. The atoms are plotted based on their positions averaged in 5 ps. α_{zz} (Å^{-1}) and α_{zx} (Å^{-1}) show the screw and edge components, respectively. In (b), the edge dislocation wanders on the slip plane during the measurement, resulting in distorted atomic columns in the plot. (e) Trajectory of the screw dislocation at an applied shear stress of 160 MPa for 40 ps at 1400 K. The time interval between two neighbouring points is 2 ps.

Figures 9b-d show the core structures of the edge and 70.5° mixed dislocations on the $\{110\}$ plane at 1000 K. Both dislocations exhibit relatively compact cores without dissociation, which are similar to those in BCC transition metals. The edge and mixed dislocations have planar cores and should have lower glide resistance than the screw core. For the mixed dislocation, the edge component is dominant with its magnitude $2\sqrt{2}$ times that of the screw component. In addition, the mixed dislocation core adopts the atom-centered (AC) structure while the BCC transition metals have the bond-centered (BC) structure

in DFT calculations (Romaner et al., 2021). These differences cannot be fully attributed to the intrinsic difference between Ti and BCC transition metals; the measurements here are based on simulations at 1000 K and DP-Ti could also produce some artefacts as seen in other interatomic potentials.

4.2. Dislocation mobilities

Figure 10 shows the velocities and mobilities of the $\langle 111 \rangle/2$ dislocations in the BCC Ti measured from MD at 1400 K. For the edge and mixed dislocations, the velocity increases almost linearly with increasing τ_{app}. We note that at such a high temperature, thermal fluctuations can influence the measured velocities at different applied stresses. Nevertheless, the current measurements still allow us to extract the mobilities with reasonable accuracies. The screw dislocation is almost stationary with a low velocity when $\tau_{\text{app}} < 80$ MPa. Above this threshold, the velocity is nearly proportional to the net shear stress $\tau_{\text{app}} - \tau_0$. Among the three cases, the edge dislocation has the highest mobility, followed closely by the mixed dislocation, which has largely the same dominant edge component. The screw dislocation has the lowest mobility at nearly 1/3 that of the edge and 40% that of the mixed dislocation. The differences in mobility here are much smaller than that in BCC transition metals (Yin et al., 2021). Since pure BCC Ti is only stable at very high temperatures, twinning and fracture are not the primary concerns and thus not studied here. Nonetheless, extension to them can be made following the methods in HCP-Ti raised to high temperatures.

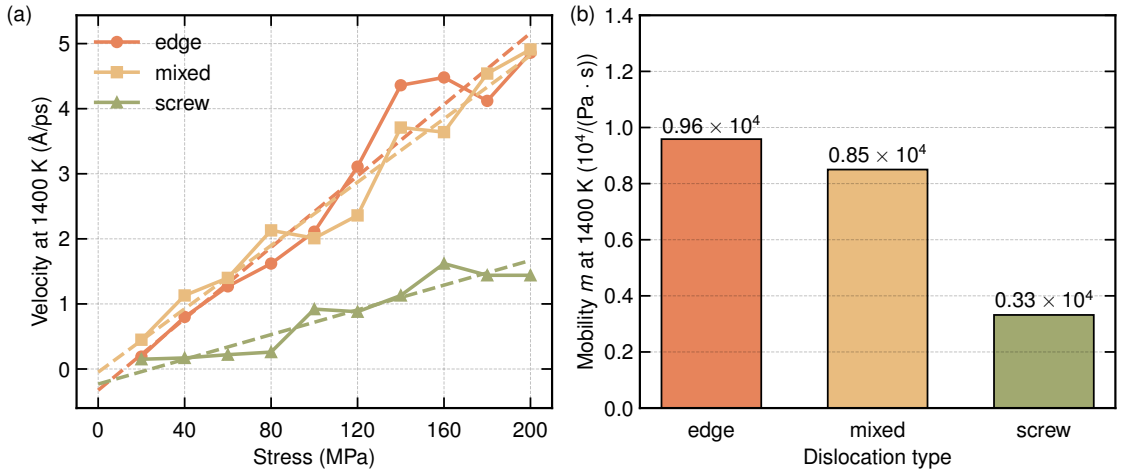

Figure 10: BCC $\langle 111 \rangle/2$ dislocation velocities and mobilities measured from MD simulations using DP-Ti at 1400 K. (a) Dislocation velocities as a function of applied shear stress. (b) Dislocation mobilities m fitted according to Eq. (5).

5. Discussion

The above results provide a complete and self-consistent understanding of crystal lattice defects and crack-tips governing plastic deformation in both HCP-α and BCC-β Ti. The fundamental dislocation core properties were studied through molecular dynamics and statics simulations with DP-Ti and supplemented by DFT calculations. All dislocation core structures and associated behaviour are consistent with a broad range of experimental observations in the literature. In particular, DP-Ti reproduces the screw $\langle \mathbf{a} \rangle$ dislocation "locking-unlocking" behaviour, which is likely intrinsic to pure Ti. Close comparisons of core structures with DFT calculations show that dislocation cores in HCP are more complex than those in BCC and FCC structures. In particular, the screw $\langle \mathbf{a} \rangle$ core exhibits multiple states on prism I wide and pyramidal I narrow planes. In each of the dissociated structures, partial dislocations adopt compact core structures which are similar to, but more complex than those of the $\langle 111 \rangle/2$ screw core in BCC structures. The complexity in core structures is perhaps a general feature in crystalline materials outside the FCC family, and should be studied using a combination of DFT and reliable atomistic potentials.

In HCP-Ti, the exact core dissociation is not solely determined by SF energies on the relevant planes. For the screw $\langle \mathbf{a} \rangle$ dislocation, DP-Ti produces one high energy and one low energy dissociation on the pyramidal I narrow plane (Fig. 1), which appears to be similar to that in DFT (Clouet et al., 2015). However, the low energy and high energy core structures are opposite to the DFT cores. Coincidentally, the spline-MEAM interatomic potential (Hennig et al., 2008) also possesses two core structures as DP-Ti, but their energy states are opposite to the DFT results as well. Attempts are being made to fit new interatomic

potentials with the correct partial core structures and energy ordering, but success has not been achieved so far. We are unaware of any interatomic potential (Chen et al., 2022; Dickel et al., 2018; Ehemann et al., 2017; Hennig et al., 2008; Kim et al., 2006; Ko et al., 2015; Mendelev et al., 2016; Sun et al., 2018) which exhibits all of the correct core structures of the screw $\langle \mathbf{a} \rangle$ dislocation in Ti. The current simulations thus demonstrate qualitative features of the glide behaviour of the screw $\langle \mathbf{a} \rangle$ dislocation. The challenge seems to be persistent and requires further study in Ti. Reproducing the exact partial cores would enable study on the screw $\langle \mathbf{a} \rangle$ cross-slip transition path (e.g., via the double-kink nucleation) and energetics of the transition between two slip planes to provide more quantitative kinetic information on the rate limiting process.

For the $\langle \mathbf{c}+\mathbf{a} \rangle$ dislocations, DP-Ti yields a $\langle \mathbf{c}+\mathbf{a} \rangle$ screw core structure and glide behaviour consistent with the new DFT calculation here. These simulations showed that the screw dislocation has a much lower energy ($\sim$134 meV/Å) when dissociated on the pyramidal I wide plane than on the pyramidal II plane. This is consistent with broad experimental observations in which the pyramidal I plane is the primary slip plane for $\langle \mathbf{c}+\mathbf{a} \rangle$ slips in Ti (Gong and Wilkinson, 2009; Kishida et al., 2020; Numakura et al., 1986; Wang et al., 2013; Zaefferer, 2003). The $\langle \mathbf{c}+\mathbf{a} \rangle$ screw dislocation is not stable on the pyramidal II plane at finite temperatures; this is not surprising since (i) the pyramidal I wide plane has a much lower metastable SF energy than the pyramidal II plane and (ii) the dissociated partial pair have nearly pure screw characters and can cross-slip independently (Wu and Curtin, 2016b). However, $\langle \mathbf{c}+\mathbf{a} \rangle$ cross-slip (Ding et al., 2014; Jones and Hutchinson, 1981) and pyramidal II $\langle \mathbf{c}+\mathbf{a} \rangle$ slip (Kwon et al., 2013; Minonishi et al., 1982, 1985; Roberts et al., 2020; Williams et al., 2002) are observed in experiments at high temperatures in Ti and Ti-based alloys. Temperature, solutes and applied stresses may thus influence the relative stability and cross-slip energy barrier.

The very high Peierls stress and low mobility of the mixed $\langle \mathbf{c}+\mathbf{a} \rangle$ dislocation are beyond expectation, even though TEM studies (Numakura et al., 1986) imply low mobility of this dislocation. It is now intriguing to inquire how $\langle \mathbf{c}+\mathbf{a} \rangle$ slip (loop expansion) occurs on the pyramidal I wide plane in Ti. In addition, the low mobility of the mixed dislocation should be taken into considerations in higher scale modelling, e.g., dislocation dynamics simulations (Aubry et al., 2016). At high temperatures (e.g., 900 K), the $\langle \mathbf{c}+\mathbf{a} \rangle$ mixed and edge dislocations are not stable against pyramidal-to-basal (PB) climb dissociations. The instabilities of the $\langle \mathbf{c}+\mathbf{a} \rangle$ mixed and edge dislocations on pyramidal I and II planes are not surprising and consistent with a previous dislocation energy analysis based on linear elasticity (Wu et al., 2016). The transition is a thermally activated process and applied stresses may have additional effects on the transition rates. Here we studied the effects of stress and provided some simulation results at a high temperature. This problem is certainly worth further study to determine the exact transition path and energy barrier. Nonetheless, the PB transition is energetically favourable and can rationalise the difficulties seen in single crystal $\langle \mathbf{c} \rangle$ axis compression experiments conducted over a wide range of temperatures (e.g., 190 K to 1000 K in Ti-6.6Al (Williams et al., 2002)). Our study further points out the necessity to conduct high resolution TEM on these dislocation core structures and their dissociations in future experimental works.

Caution should be exercised when interpreting the apparent CRSS τ_0 and dislocation mobilities at finite temperatures, in both simulations and experiments. During constant strain rate deformation, dislocation glides with some fixed velocities following the Orowan equation: $\dot{\varepsilon} = \rho b \bar{v}$, where ρ and $\bar{v}$ are the mobile dislocation density and mean velocity. So $\bar{v}$ is a definite function of $\dot{\varepsilon}$ at constant ρ. To satisfy the imposed strain rate, the applied stress τ_{app} will follow the plastic response of the material to drive $\bar{v}$ or ρ via reduced glide barriers (Eq. 4). Therefore, the constant-stress dislocation velocity measurement simulations here provide the variation of $\bar{v}$ with respect to the applied strain rate in the phonon drag regime. The effects of stresses or strain-rate require further study in the lower stress, nucleation dominant regime.

In addition, we also determine the twin boundary structures and energies in HCP Ti, which agree very well with DFT calculations. In the BCC structure, the $\langle 111 \rangle/2$ dislocation core structures and glide behaviour were determined at very high temperatures where the BCC phase is metastable or stable. These complete, atomistic-based results can provide key inputs to meso-scale simulations. Specifically, the active slip system, critical resolved shear stress and dislocation mobility are important material parameters used in dislocation dynamics simulations.

6. Conclusions

In summary, we performed a comprehensive study on all important dislocation, twinning and crack systems in HCP and BCC Ti, using a fine-tuned machine learning Deep Potential for Ti (DP-Ti), large-scale DFT calculations and fracture mechanics theory. The $\langle \mathbf{a} \rangle$, $\langle \mathbf{c}+\mathbf{a} \rangle$ and $\langle \mathbf{c} \rangle$ dislocation core structures, their dissociations on competing planes and relative energetics were quantitatively determined using DP-Ti. In particular, we demonstrate the "locking-unlocking" behaviour of the screw $\langle \mathbf{a} \rangle$ dislocation in explicit

molecular dynamics simulations when the pyramidal I narrow plane is the stable ground state plane. In BCC Ti, we presented the first reliable predictions of dislocation core structures and glide behaviour. In addition, we determine the critical resolved shear stresses and mobilities of the different dislocations at 0 K and 300 K for HCP-Ti, and higher temperatures for BCC Ti. These results are broadly consistent with available DFT calculations and previous experiments, and thus provide a quantitative understanding on the complex plastic deformation mechanisms in Ti. The current work also reveals some unexpected properties of the mixed $\langle \mathbf{c} + \mathbf{a} \rangle$ dislocation on the pyramidal I plane, which points to possible future experiment validations.

The intrinsic dislocation behaviour can serve as a basis for studying the effects of applied stresses and alloying in Ti. For example, Ti can be stabilised in the BCC structure at room temperature via alloying with transition metals such as V. The effects of V solutes on dislocation and twinning behaviour can be studied and compared with the results in the current work. Nevertheless, accurate interatomic potentials for alloys remain one of the main barriers to predictive modelling of fundamental dislocation and twinning behaviour in BCC and HCP structures. Recent machine learning approaches, including the DP-Ti here, have demonstrated some successes in capturing most of the core structures in both BCC and HCP systems. However, Ti appears to be particularly complex, as seen in the difficulties in reproducing the energy ordering of the various screw $\langle \mathbf{a} \rangle$ dislocation dissociations. Given the importance of Ti and the need for atomistic modelling beyond DFT scales, additional efforts, such as developing new machine learning or classical interatomic potentials, are being made to address this long standing issue and eventually enable true predictive modelling of plasticity and fracture in Ti and Ti alloys.

CRediT authorship contribution statement

T.W.: Methodology, Formal analysis, Writing. A.L.: Methodology, Formal analysis. R.W.: Methodology, Formal analysis. L.Z.: Methodology, Resources, Software. J.H.: Methodology, Formal analysis. H.W.: Methodology, Formal analysis, Software. D.J.S.: Formal analysis, Writing, Project administration. Z.W.: Conceptualization, Methodology, Formal analysis, Writing, Project administration.

Declaration of competing interest

The authors declare no competing interests.

Data availability

The DP-Ti model is available at https://aissquare.com/workflows/detail?pageType=models&name=Ti-model. Other data will be made available on request.

Acknowledgements

The work of T.W., A.L., R.W., D.J.S. and Z.W. is supported by the Research Grants Council, Hong Kong SAR through the Collaborative Research Fund (8730054) and Early Career Scheme Fund (21205019, Z.W.). T.W. acknowledges additional support by The University of Hong Kong (HKU) via a seed fund (2201100392). The work of H.W. is supported by the National Science Foundation of China (Grant No. 11871110 and 12122103). L.Z. acknowledges support of the Beijing Academy of Artificial Intelligence. We are grateful for Drs. Wanrun Jiang, Yinan Wang, Xiaoyang Wang, and Fuzhi Dai for helpful discussions on DP model training and dislocation properties. Computational resources are provided by the research computing facilities offered by Information Technology Services, HKU, Computing Services Centre, City University of Hong Kong, and Bohrium Cloud Platform at DP Technology.

References

Ahmadikia, B., Wang, L., Arul Kumar, M., Beyerlein, I.J., 2023. Grain boundary slip - twin transmission in titanium. Acta Materialia 244, 118556. doi:10.1016/j.actamat.2022.118556.

Albrecht, C., Hunter, A., Kumar, A., Beyerlein, I.J., 2020. A phase field model for dislocations in hexagonal close packed crystals. Journal of the Mechanics and Physics of Solids 137, 103823. doi:10.1016/j.jmps.2019.103823.

Anderson, P.M., Hirth, J.P., Lothe, J., 2017. Theory of Dislocations. Cambridge University Press. URL: https://books.google.com.sg/books?id=LK7DDQAAQBAJ.

Andric, P., Curtin, W., 2017. New theory for mode I crack-tip dislocation emission. Journal of the Mechanics and Physics of Solids 106, 315–337. doi:10.1016/j.jmps.2017.06.006.

Aubry, S., Rhee, M., Hommes, G., Bulatov, V.V., Arsenlis, A., 2016. Dislocation dynamics in hexagonal close-packed crystals. Journal of the Mechanics and Physics of Solids 94, 105–126. doi:10.1016/j.jmps.2016.04.019.

Bache, M.R., 2003. A review of dwell sensitive fatigue in titanium alloys: the role of microstructure, texture and operating conditions. International Journal of Fatigue 25, 1079–1087. doi:10.1016/S0142-1123(03)00145-2.

Bahl, S., Suwas, S., Chatterjee, K., 2021. Comprehensive review on alloy design, processing, and performance of β titanium alloys as biomedical materials. International Materials Reviews 66, 114–139. doi:10.1080/09506608.2020.1735829.

Banerjee, D., Williams, J.C., 2013. Perspectives on titanium science and technology. Acta Materialia 61, 844–879. doi:10.1016/j.actamat.2012.10.043.

Beyerlein, I.J., Zhang, X., Misra, A., 2014. Growth twins and deformation twins in metals. Annual Review of Materials Research 44, 329–363. doi:10.1146/annurev-matsci-070813-113304.

Blöchl, P.E., 1994. Projector augmented-wave method. Physical Review B 50, 17953–17979. doi:10.1103/PhysRevB.50.17953.

Bulatov, V., Cai, W., 2006. Computer Simulations of Dislocations. Oxford University Press, USA. doi:10.1093/oso/9780198526148.001.0001.

Castany, P., Besse, M., Gloriant, T., 2012. In situ TEM study of dislocation slip in a metastable β titanium alloy. Scripta Materialia 66, 371–373. doi:10.1016/j.scriptamat.2011.11.036.

Castany, P., Pettinari-Sturmel, F., Crestou, J., Douin, J., Coujou, A., 2007. Experimental study of dislocation mobility in a Ti–6Al–4V alloy. Acta Materialia 55, 6284–6291. doi:10.1016/j.actamat.2007.07.032.

Chen, S., Aitken, Z.H., Sorkin, V., Yu, Z.G., Wu, Z., Zhang, Y.W., 2022. Modified embedded-atom method potentials for the plasticity and fracture behaviors of unary hcp metals. Advanced Theory and Simulations 5, 2100377. doi:10.1002/adts.202100377.

Cheng, B., Ngan, A.H.W., 2013. The crystal structures of sintered copper nanoparticles: A molecular dynamics study. International Journal of Plasticity 47, 65–79. doi:10.1016/j.ijplas.2013.01.006.

Chong, Y., Poschmann, M., Zhang, R., Zhao, S., Hooshmand, M.S., Rothchild, E., Olmsted, D.L., Morris, J.W., Chrzan, D.C., Asta, M., Minor, A.M., 2020. Mechanistic basis of oxygen sensitivity in titanium. Science Advances 6. doi:10.1126/sciadv.abc4060.

Clouet, E., Caillard, D., Chaari, N., Onimus, F., Rodney, D., 2015. Dislocation locking versus easy glide in titanium and zirconium. Nature Materials 14, 931–936. doi:10.1038/nmat4340.

Dickel, D.E., Baskes, M.I., Aslam, I., Barrett, C.D., 2018. New interatomic potential for Mg–Al–Zn alloys with specific application to dilute Mg-based alloys. Modelling and Simulation in Materials Science and Engineering 26, 045010. doi:10.1088/1361-651x/aabaad.

Ding, R., Gong, J., Wilkinson, A.J., Jones, I.P., 2014. $\langle c+a \rangle$ dislocations in deformed Ti–6Al–4V micro-cantilevers. Acta Materialia 76, 127–134. doi:10.1016/j.actamat.2014.05.010.

DP for Ti at AIS Square, 2023. URL: https://aissquare.com/workflows/detail?pageType=models&name=Ti-model.

Ehemann, R.C., Nicklas, J.W., Park, H., Wilkins, J.W., 2017. *Ab initio* based empirical potential applied to tungsten at high pressure. Physical Review B 95, 184101–. doi:10.1103/PhysRevB.95.184101.

Faken, D., Jónsson, H., 1994. Systematic analysis of local atomic structure combined with 3D computer graphics. Computational Materials Science 2, 279–286. doi:10.1016/0927-0256(94)90109-0.

Farrokh, B., Khan, A.S., 2009. Grain size, strain rate, and temperature dependence of flow stress in ultra-fine grained and nanocrystalline cu and al: Synthesis, experiment, and constitutive modeling. International Journal of Plasticity 25, 715–732. doi:10.1016/j.ijplas.2008.08.001.

Gao, J., Huang, Y., Guan, D., Knowles, A.J., Ma, L., Dye, D., Rainforth, W.M., 2018. Deformation mechanisms in a metastable beta titanium twinning induced plasticity alloy with high yield strength and high strain hardening rate. Acta Materialia 152, 301–314. doi:10.1016/j.actamat.2018.04.035.

Ghazisaeidi, M., Hector Jr, L.G., Curtin, W.A., 2014. First-principles core structures of $\langle c+a \rangle$ edge and screw dislocations in Mg. Scripta Materialia 75, 42–45. doi:10.1016/j.scriptamat.2013.11.013.

Ghazisaeidi, M., Trinkle, D., 2012. Core structure of a screw dislocation in Ti from density functional theory and classical potentials. Acta Materialia 60, 1287–1292. doi:10.1016/j.actamat.2011.11.024.

Ghosh, S., Shahba, A., Tu, X., Huskins, E.L., Schuster, B.E., 2016. Crystal plasticity FE modeling of Ti alloys for a range of strain-rates. Part II: Image-based model with experimental validation. International Journal of Plasticity 87, 69–85. doi:10.1016/j.ijplas.2016.09.003.

Gong, J., Wilkinson, A.J., 2009. Anisotropy in the plastic flow properties of single-crystal α titanium determined from micro-cantilever beams. Acta Materialia 57, 5693–5705. doi:10.1016/j.actamat.2009.07.064.

Griffith, A.A., 1921. VI. The phenomena of rupture and flow in solids. Philosophical Transactions of the Royal Society of London. Series A 221, 163–198. doi:10.1098/rsta.1921.0006.

Hartley, C.S., Mishin, Y., 2005. Characterization and visualization of the lattice misfit associated with dislocation cores. Acta Materialia 53, 1313–1321. doi:10.1016/j.actamat.2004.11.027.

Hennig, R.G., Lenosky, T.J., Trinkle, D.R., Rudin, S.P., Wilkins, J.W., 2008. Classical potential describes martensitic phase transformations between the α, β, and ω titanium phases. Physical Review B 78, 054121–10. doi:10.1103/PhysRevB.78.054121.

Hooshmand, H.S., Zhang, R., Chong, Y., Chen, E., Frolov, T., Olmsted, D.L., Minor, A.M., Asta, M., 2021. Twin-boundary structural phase transitions in elemental titanium. Arxiv doi:10.48550/arXiv.2103.06194.

Hooshmand, M.S., Mills, M.J., Ghazisaeidi, M., 2017. Atomistic modeling of dislocation interactions with twin boundaries in Ti. Modelling and Simulation in Materials Science and Engineering 25, 045003. doi:10.1088/1361-651X/aa6323.

Iftikhar, C.M.A., Brahme, A., Inal, K., Khan, A.S., 2022. An evolution of subsequent yield loci under proportional and non-proportional loading path of 'as-received' extruded AZ31 magnesium alloy: Experiments and CPFEM modeling. International Journal of Plasticity 151, 103216. doi:10.1016/j.ijplas.2022.103216.

Itakura, M., Kaburaki, H., Yamaguchi, M., Tsuru, T., 2016. Novel cross-slip mechanism of pyramidal screw dislocations in magnesium. Physical Review Letters 116, 225501–5. doi:10.1103/PhysRevLett.116.225501.

Jones, I.P., Hutchinson, W.B., 1981. Stress-state dependence of slip in Titanium-6Al-4V and other H.C.P. metals. Acta Metallurgica 29, 951–968. doi:10.1016/0001-6160(81)90049-3.

Junge, T., Molinari, J.F., 2014. Plastic activity in nanoscratch molecular dynamics simulations of pure aluminium. International Journal of Plasticity 53, 90–106. doi:10.1016/j.ijplas.2013.07.005.

Kadkhodaei, S., Hong, Q.J., van de Walle, A., 2017. Free energy calculation of mechanically unstable but dynamically stabilized bcc titanium. Physical Review B 95, 064101. doi:10.1103/physrevb.95.064101.

Khan, A.S., Huang, S., 1992. Experimental and theoretical study of mechanical behavior of 1100 aluminum in the strain rate range

10^{-5}–10^{4} s^{-1}. International Journal of Plasticity 8, 397–424. doi:10.1016/0749-6419(92)90057-J.
Khan, A.S., Kazmi, R., Farrokh, B., 2007. Multiaxial and non-proportional loading responses, anisotropy and modeling of Ti–6Al–4V titanium alloy over wide ranges of strain rates and temperatures. International Journal of Plasticity 23, 931–950. doi:10.1016/j.ijplas.2006.08.006.
Khan, A.S., Liang, R., 1999. Behaviors of three BCC metal over a wide range of strain rates and temperatures: experiments and modeling. International Journal of Plasticity 15, 1089–1109. doi:10.1016/S0749-6419(99)00030-3.
Khan, A.S., Sung Suh, Y., Kazmi, R., 2004. Quasi-static and dynamic loading responses and constitutive modeling of titanium alloys. International Journal of Plasticity 20, 2233–2248. doi:10.1016/j.ijplas.2003.06.005.
Khan, A.S., Yu, S., Liu, H., 2012. Deformation induced anisotropic responses of Ti–6Al–4V alloy Part II: A strain rate and temperature dependent anisotropic yield criterion. International Journal of Plasticity 38, 14–26. doi:10.1016/j.ijplas.2012.03.013.
Khan, A.S., Zhang, H., 2000. Mechanically alloyed nanocrystalline iron and copper mixture: behavior and constitutive modeling over a wide range of strain rates. International Journal of Plasticity 16, 1477–1492. doi:10.1016/S0749-6419(00)00024-3.
Kim, Y.M., Lee, B.J., Baskes, M.I., 2006. Modified embedded-atom method interatomic potentials for Ti and Zr. Physical Review B 74, 014101–12. doi:10.1103/PhysRevB.74.014101.
Kishida, K., Kim, J.G., Nagae, T., Inui, H., 2020. Experimental evaluation of critical resolved shear stress for the first-order pyramidal c + a slip in commercially pure Ti by micropillar compression method. Acta Materialia 196, 168–174. doi:10.1016/j.actamat.2020.06.043.
Ko, W.S., Grabowski, B., Neugebauer, J., 2015. Development and application of a Ni-Ti interatomic potential with high predictive accuracy of the martensitic phase transition. Physical Review B 92, 134107. doi:10.1103/PhysRevB.92.134107.
Kresse, G., Furthmüller, J., 1996. Efficient iterative schemes forab initiototal-energy calculations using a plane-wave basis set. Physical Review B 54, 11169–11186. doi:10.1103/physrevb.54.11169.
Kumar, A., Wang, J., Tomé, C.N., 2015. First-principles study of energy and atomic solubility of twinning-associated boundaries in hexagonal metals. Acta Materialia 85, 144–154. doi:10.1016/j.actamat.2014.11.015.
Kwasniak, P., Clouet, E., 2019. Basal slip of $\langle a \rangle$ screw dislocations in hexagonal titanium. Scripta Materialia 162, 296–299. doi:10.1016/j.scriptamat.2018.11.027.
Kwon, J., Brandes, M.C., Sudharshan Phani, P., Pilchak, A.P., Gao, Y.F., George, E.P., Pharr, G.M., Mills, M.J., 2013. Characterization of deformation anisotropies in an α-Ti alloy by nanoindentation and electron microscopy. Acta Materialia 61, 4743–4756. doi:10.1016/j.actamat.2013.05.005.
Lane, N.J., Simak, S.I., Mikhaylushkin, A.S., Abrikosov, I.A., Hultman, L., Barsoum, M.W., 2011. First-principles study of dislocations in hcp metals through the investigation of the $\{11\bar{2}1\}$ twin boundary. Physical Review B 84. doi:10.1103/physrevb.84.184101.
Levine, E.D., 1966. Deformation mechanisms in titanium at low temperatures. Transactions of the Metallurgical Society of AIME 236, 1558–1569.
Lhadi, S., Berbenni, S., Gey, N., Richeton, T., Germain, L., 2018. Micromechanical modeling of the effect of elastic and plastic anisotropies on the mechanical behavior of β-ti alloys. International Journal of Plasticity 109, 88–107. doi:10.1016/j.ijplas.2018.05.010.
Liu, J., Khan, A.S., Takacs, L., Meredith, C.S., 2015. Mechanical behavior of ultrafine-grained/nanocrystalline titanium synthesized by mechanical milling plus consolidation: Experiments, modeling and simulation. International Journal of Plasticity 64, 151–163. doi:10.1016/j.ijplas.2014.08.007.
Lu, D., Jiang, W., Chen, Y., Zhang, L., Jia, W., Wang, H., Chen, M., 2022. DP compress: A model compression scheme for generating efficient deep potential models. Journal of Chemical Theory and Computation 18, 5559–5567. doi:10.1021/acs.jctc.2c00102.
Marchenko, A., Mazière, M., Forest, S., Strudel, J.L., 2016. Crystal plasticity simulation of strain aging phenomena in α-titanium at room temperature. International Journal of Plasticity 85, 1–33. doi:10.1016/j.ijplas.2016.05.007.
Mendelev, M.I., Underwood, T.L., Ackland, G.J., 2016. Development of an interatomic potential for the simulation of defects, plasticity, and phase transformations in titanium. The Journal of Chemical Physics 145, 154102. doi:10.1063/1.4964654.
Mendis, B.G., Mishin, Y., Hartley, C.S., Hemker, K.J., 2006. Use of the Nye tensor in analyzing HREM images of bcc screw dislocations. Philosophical Magazine 86, 4607–4640. doi:10.1080/14786430600660849.
Methfessel, M., Paxton, A.T., 1989. High-precision sampling for Brillouin-zone integration in metals. Physical Review B 40, 3616–3621. doi:10.1103/physrevb.40.3616.
Minonishi, Y., Morozumi, S., Yoshinaga, H., 1982. $\{11\bar{2}2\}\langle\bar{1}\bar{1}23\rangle$ slip in titanium. Scripta Metallurgica 16, 427–430. doi:10.1016/0036-9748(82)90166-1.
Minonishi, Y., Morozumi, S., Yoshinaga, H., 1985. Accommodation around $\{10\bar{1}1\}$ twins in titanium. Scripta Metallurgica 19, 1241–1245. doi:10.1016/0036-9748(85)90246-7.
Monkhorst, H.J., Pack, J.D., 1976. Special points for Brillouin-zone integrations. Physical Review B 13, 5188–5192. doi:10.1103/PhysRevB.13.5188.
Mouhat, F., Coudert, F.X., 2014. Necessary and sufficient elastic stability conditions in various crystal systems. Physical Review B 90, 224104–4. doi:10.1103/physrevb.90.224104.
Numakura, H., Minonishi, Y., Koiwa, M., 1986. $\langle\bar{1}\bar{1}23\rangle\{10\bar{1}1\}$ slip in titanium polycrystals at room temperature. Scripta Metallurgica 20, 1581–1586. doi:10.1016/0036-9748(86)90399-6.
Olmsted, D.L., HectorJr, L.G., Curtin, W.A., Clifton, R.J., 2005. Atomistic simulations of dislocation mobility in Al, Ni and Al/Mg alloys. Modelling and Simulation in Materials Science and Engineering 13, 371–388. doi:10.1088/0965-0393/13/3/007.
Perdew, J.P., Burke, K., Ernzerhof, M., 1996. Generalized gradient approximation made simple. Physical Review Letters 77, 3865–3868. doi:10.1103/physrevlett.77.3865.
Peters, M., Kumpfert, J., Ward, C.H., Leyens, C., 2003. Titanium alloys for aerospace applications. Advanced Engineering Materials 5, 419–427. doi:10.1002/adem.200310095.
Poschmann, M., Asta, M., Chrzan, D.C., 2018. Convergence of calculated dislocation core structures in hexagonal close packed titanium. Modelling and Simulation in Materials Science and Engineering 26, 014003. doi:10.1088/1361-651x/aa9ba9.
Qin, Z., Wang, R., Li, S., Wen, T., Yin, B., Wu, Z., 2022. MEAM interatomic potential for thermodynamic and mechanical properties of lithium allotropes. Computational Materials Science 214, 111706. doi:10.1016/j.commatsci.2022.111706.
Rao, S.I., Venkateswaran, A., Letherwood, M.D., 2013. Molecular statics and molecular dynamics simulations of the critical stress for motion of $a/3\langle11\bar{2}0\rangle$ screw dislocations in α-Ti at low temperatures using a modified embedded atom method potential. Acta Materialia 61, 1904–1912. doi:10.1016/j.actamat.2012.12.011.

Rice, J.R., 1992. Dislocation nucleation from a crack tip: An analysis based on the Peierls concept. Journal of the Mechanics and Physics of Solids 40, 239–271. doi:10.1016/S0022-5096(05)80012-2.
Rida, A., Rao, S.I., El-Awady, J.A., 2022. Characteristics of $\langle a \rangle$ screw dislocations and their slip on prismatic and pyramidal planes in pure α titanium from atomistic simulations. Materialia 24, 101503. doi:10.1016/j.mtla.2022.101503.
Roberts, W., Gong, J., Wilkinson, A.J., Tarleton, E., 2020. Tension–compression asymmetry of $\langle c + a \rangle$ slip in Ti–6Al. Scripta Materialia 178, 119–123. doi:10.1016/j.scriptamat.2019.11.002.
Romaner, L., Pradhan, T., Kholtobina, A., Drautz, R., Mrovec, M., 2021. Theoretical investigation of the 70.5° mixed dislocations in body-centered cubic transition metals. Acta Materialia 217, 117154. doi:10.1016/j.actamat.2021.117154.
Romero, R.A., Xu, S., Jian, W.R., Beyerlein, I.J., Ramana, C.V., 2022. Atomistic simulations of the local slip resistances in four refractory multi-principal element alloys. International Journal of Plasticity 149, 103157. doi:10.1016/j.ijplas.2021.103157.
Shahba, A., Ghosh, S., 2016. Crystal plasticity FE modeling of Ti alloys for a range of strain-rates. Part I: A unified constitutive model and flow rule. International Journal of Plasticity 87, 48–68. doi:10.1016/j.ijplas.2016.09.002.
Sun, S., Ramachandran, B.R., Wick, C.D., 2018. Solid, liquid, and interfacial properties of TiAl alloys: parameterization of a new modified embedded atom method model. Journal of Physics: Condensed Matter 30, 075002. doi:10.1088/1361-648x/aaa52c.
Sun, Y., Beltz, G.E., 1994. Dislocation nucleation from a crack tip: A formulation based on anisotropic elasticity. Journal of the Mechanics and Physics of Solids 42, 1905–1932. doi:10.1016/0022-5096(94)90018-3.
Tesař, K., Koller, M., Vokoun, D., Tyc, O., Čech, J., Sedlák, P., 2023. Texture, elastic anisotropy and thermal stability of commercially pure titanium prepared by room temperature ECAP. Materials & Design 226, 111678. doi:10.1016/j.matdes.2023.111678.
Thompson, A.P., Aktulga, H.M., Berger, R., Bolintineanu, D.S., Brown, W.M., Crozier, P.S., in 't Veld, P.J., Kohlmeyer, A., Moore, S.G., Nguyen, T.D., Shan, R., Stevens, M.J., Tranchida, J., Trott, C., Plimpton, S.J., 2022. LAMMPS - a flexible simulation tool for particle-based materials modeling at the atomic, meso, and continuum scales. Computer Physics Communications 271, 108171. doi:10.1016/j.cpc.2021.108171.
Tsuru, T., Itakura, M., Yamaguchi, M., Watanabe, C., Miura, H., 2022. Dislocation core structure and motion in pure titanium and titanium alloys: A first-principles study. Computational Materials Science 203, 111081. doi:10.1016/j.commatsci.2021.111081.
Vítek, V., Perrin, R.C., Bowen, D.K., 1970. The core structure of $1/2\langle 111 \rangle$ screw dislocations in b.c.c. crystals. Philosophical Magazine A 21, 1049–1073. doi:10.1080/14786437008238490.
Wang, H., Zhang, L., Han, J., E, W., 2018a. DeePMD-kit: A deep learning package for many-body potential energy representation and molecular dynamics. Computer Physics Communications 228, 178–184. doi:10.1016/j.cpc.2018.03.016.
Wang, J., Zecevic, M., Knezevic, M., Beyerlein, I.J., 2020. Polycrystal plasticity modeling for load reversals in commercially pure titanium. International Journal of Plasticity 125, 294–313. doi:10.1016/j.ijplas.2019.09.013.
Wang, L., Barabash, R., Bieler, T., Liu, W., Eisenlohr, P., 2013. Study of $\{11\bar{2}1\}$ twinning in α-Ti by EBSD and Laue microdiffraction. Metallurgical and Materials Transactions A 44, 3664–3674. doi:10.1007/s11661-013-1714-y.
Wang, P., Liu, F., Cui, Y., Liu, Z., Qu, S., Zhuang, Z., 2018b. Interpreting strain burst in micropillar compression through instability of loading system. International Journal of Plasticity 107, 150–163. doi:10.1016/j.ijplas.2018.04.002.
Wang, R., Ma, X., Zhang, L., Wang, H., Srolovitz, D.J., Wen, T., Wu, Z., 2022a. Classical and machine learning interatomic potentials for BCC vanadium. Physical Review Materials 6, 113603. doi:10.1103/physrevmaterials.6.113603.
Wang, R., Zhu, L., Pattamatta, S., J., S.D., Wu, Z., 2022b. The taming of the screw: Dislocation cores in BCC metals and alloys. arXiv: doi:10.48550/arXiv.2209.12323.
Wen, T., Wang, R., Zhu, L., Zhang, L., Wang, H., Srolovitz, D.J., Wu, Z., 2021. Specialising neural network potentials for accurate properties and application to the mechanical response of titanium. npj Computational Materials 7, 206–11. doi:10.1038/s41524-021-00661-y.
Williams, J.C., Baggerly, R.G., Paton, N.E., 2002. Deformation behavior of HCP Ti-Al alloy single crystals. Metallurgical and Materials Transactions A 33, 837–850. doi:10.1007/s11661-002-0153-y.
Wu, Z., Curtin, W.A., 2015a. Brittle and ductile crack-tip behavior in magnesium. Acta Materialia 88, 1–12. doi:10.1016/j.actamat.2015.01.023.
Wu, Z., Curtin, W.A., 2015b. The origins of high hardening and low ductility in magnesium. Nature 526, 62–67. doi:10.1038/nature15364.
Wu, Z., Curtin, W.A., 2016a. Intrinsic structural transitions of the pyramidal I $\langle c + a \rangle$ dislocation in magnesium. Scripta Materialia 116, 104–107. doi:10.1016/j.scriptamat.2016.01.041.
Wu, Z., Curtin, W.A., 2016b. Mechanism and energetics of $\langle c + a \rangle$ dislocation cross-slip in hcp metals. Proceedings of the National Academy of Sciences 113, 11137–11142. doi:10.1073/pnas.1603966113.
Wu, Z., Yin, B., Curtin, W.A., 2016. Energetics of dislocation transformations in hcp metals. Acta Materialia 119, 203–217. doi:10.1016/j.actamat.2016.08.002.
Xiao, J., Zhu, L., Wang, R., Deng, C., Wu, Z., Zhu, Y., 2023. Unveiling deformation twin nucleation and growth mechanisms in BCC transition metals and alloys. Materials Today , in–pressdoi:10.1016/j.mattod.2023.03.028.
Xu, Y., Fox, K., Rugg, D., Dunne, F.P.E., 2020. Cyclic plasticity and thermomechanical alleviation in titanium alloys. International Journal of Plasticity 134, 102753. doi:10.1016/j.ijplas.2020.102753.
Yazar, K.U., Mishra, S., Kumar, L., Bahl, S., Kiran Kumar, T., Suwas, S., 2022. Texture induced planar anisotropy of dwell fatigue response in titanium: Insights from experiments and crystal plasticity simulations. International Journal of Plasticity 152, 103140. doi:10.1016/j.ijplas.2021.103140.
Yin, B., Wu, Z., Curtin, W.A., 2017. Comprehensive first-principles study of stable stacking faults in hcp metals. Acta Materialia 123, 223–234. doi:10.1016/j.actamat.2016.10.042.
Yin, S., Zuo, Y., Abu-Odeh, A., Zheng, H., Li, X.G., Ding, J., Ong, S.P., Asta, M., Ritchie, R.O., 2021. Atomistic simulations of dislocation mobility in refractory high-entropy alloys and the effect of chemical short-range order. Nature communications 12, 4873. doi:10.1038/s41467-021-25134-0.
Yu, Q., Qi, L., Tsuru, T., Traylor, R., Rugg, D., Morris, J.W., Asta, M., Chrzan, D.C., Minor, A.M., 2015. Origin of dramatic oxygen solute strengthening effect in titanium. Science 347, 635–639. doi:10.1126/science.1260485.
Yu, Q., Sun, J., Morris Jr., J.W., Minor, A.M., 2013. Source mechanism of non-basal $\langle c + a \rangle$ slip in Ti alloy. Scripta Materialia 69, 57–60. doi:10.1016/j.scriptamat.2013.03.009.

Zaefferer, S., 2003. A study of active deformation systems in titanium alloys: dependence on alloy composition and correlation with deformation texture. Materials Science and Engineering: A 344, 20–30. doi:10.1016/S0921-5093(02)00421-5.

Zhang, R., Zhao, S., Ophus, C., Deng, Y., Vachhani, S.J., Ozdol, B., Traylor, R., Bustillo, K.C., Morris, J.W., Chrzan, D.C., Asta, M., Minor, A.M., 2019. Direct imaging of short-range order and its impact on deformation in Ti-6Al. Science Advances 5, eaax2799. doi:10.1126/sciadv.aax2799.

Zhao, S., Zhang, R., Yu, Q., Ell, J., Ritchie, R.O., Minor, A.M., 2021. Cryoforged nanotwinned titanium with ultrahigh strength and ductility. Science 373, 1363–1368. doi:10.1126/science.abe7252.